INL/EXT-20-60135

AFIP6-MkII and RERTR-12 Porosity Data Collection and Analysis for Modeling and Simulation

Kelley Verner, Charlyne Smith, Dennis D. Keiser, Jr., Assel Aitkaleyva, Benjamin Beeler, and Brandon Miller

April 2020

The INL is a U.S. Department of Energy National Laboratory
operated by Battelle Energy Alliance

AFIP6-MkII and RERTR-12 Porosity Data Collection and Analysis for Modeling and Simulation

Kelley Verner, Charlyne Smith, Dennis D. Keiser, Jr., Assel Aitkaleyva, Benjamin Beeler, and Brandon Miller

April 2020

Idaho National Laboratory
Idaho Falls, Idaho 83415

AFIP6-MkII and RERTR-12 Porosity Data Collection and Analysis for Modeling and Simulation

Kelley Verner, Charlyne Smith, Dennis D. Keiser, Jr., Assel Aitkaleyva, Benjamin Beeler, and Brandon Miller

April 2020

Approved by:

James I. Cole Approving Manager	Date
Dennis D. Keiser, Jr. Peer Reviewer	Date
Benjamin W. Beeler Peer Reviewer	Date

SUMMARY

Gathering data for the improvement of nuclear fuel modeling and simulation efforts is the primary driver for this work. Mechanistic models allow for a better understanding of the material on a micro and macrostructural level while saving time and money over traditional experiment efforts. Historically, summarized data and correlations are the inputs for empirical material models and model validation. When improving these models for nuclear fuels with experimental results, there is a lack of reliable data readily available. Experiments - RERTR-12 and AFIP6-MkII - were conducted to understand the irradiation behavior of metallic U-10Mo monolithic fuels for use in extreme reactor environments such as research reactors like the Advanced Test Reactor (ATR) or the High Flux Isotope Reactor. Microstructural characteristics of fission gas pores (FGP) in each experiment are collected using an automated image analysis technique developed at the University of Florida and presented here. A series of statistical tests are performed to explore the reliability of the results, as well as understand where the data is lacking and what future data collection is necessary to provide sufficient information to assist modeling efforts. The focus is on the porosity, pore size, and eccentricity of FGPs formed during irradiation in three AFIP6-MkII samples and one RERTR-12 sample. From the analysis, it is clear there are substantial impacts of fission density on the pore structure, but there also exist underlying connections between each sample and the behavior observed in the pores. Further analyses of the pre- and post-irradiation microstructure are needed to improve the understanding of these connections. An early method for microstructural data analysis is presented within and is currently being expanded to include other microstructure data.

CONTENTS

FIGURES

TABLES

ACRONYMS

AFIP ATR Full-size plate in center flux trap position
ATR Advanced Test Reactor
BSE backscattered electrons
FGB fission gas bubbles
FGP-GUI fission gas pore graphical user interface
HEU high enriched uranium
HIP hot-isostatic pressing
INL Idaho National Laboratory
LEU low enriched uranium
M^3 Office of Materials Management and Minimization
MM Microstructural Modeling
NNSA National Nuclear Security Administration
PIE post-irradiation examination
RERTR Reduced Enrichment for Research and Test Reactors
TEM transmission electron microscopy
USHPRR U.S. High-Performance Research Reactor

AFIP6-MkII and RERTR-12 Porosity Data Collection and Analysis for Modeling and Simulation

1. INTRODUCTION

The Reduced Enrichment of Research and Test Reactors (RERTR) program began in the late 1970s, intending to reduce the enrichment of ^{235}U in the fuel used to operate research and test reactors around the world. Now, as a part of the Office of Materials Management and Minimization (M^3) in the National Nuclear Security Administration (NNSA), this work continues to focus on exploring alternative fuel types and the behavior of these fuels for the conversion from high enriched uranium (HEU) fuels to low enriched uranium (LEU) [1]. Uranium-molybdenum (U-Mo) is a promising contender for these possible LEU fuel alloys [2]. U-10wt% Mo alloy (U-10Mo), specifically, is studied intensely for use in the U.S. High-Performance Research Reactor (USPRR) program as part of M^3 goals [3].

Metallic fuels are high-density materials capable of reaching fission densities required by various reactors currently using HEU fuel. Two primary metallic fuel types are of interest for the aforementioned programs: monolithic fuels and dispersion fuels. Dispersion fuels reach densities of 8.5 gU/cm^3 while monolithic fuels used for applications requiring higher densities of the fissile material can reach densities of ~15.5 gU/cm^3 [2, 3].

Historically, swelling of metallic fuels has been a significant concern for the safety of these materials due to the fact that they were employed at relatively high temperatures [4, 5]. However, at relatively low temperatures the swelling is more stable. Microstructural grain refinement, fission gas bubbles, and phase growth impact the swelling phenomena. These microstructural features are all interdependent. To better understand the behavior of the material, the relationships between the microstructural features must also be recognized. Correlations and dependencies of one microstructural feature on another are derived by gathering data from the separate features at various fission densities. This work looks more thoroughly into these relationships and possible effects that one condition may have on another in the resulting microstructure regarding the porosity development in monolithic U-Mo alloy fuels.

The development of fission gas bubbles (FGB) in the irradiated fuel matrix lead to swelling and possibly to fuel failure [6]. Several aspects of the porosity in the U-Mo fuel matrix were studied for this report to understand the possible relationship of these FGB to other fuel behaviors. The resulting porosity, pore size, and pore size distribution in the fuel matrix of two experiments (RERTR-12 and AFIP6-MkII) are presented within. Micrographs of each sample were analyzed using an image characterization technique developed by the University of Florida [7]. Briefly, the grain size, phase decomposition, Mo homogeneity, and carbide fraction are also included in the analysis to give more context to the other microstructural features of the experiments. The data analyzed and gathered intends to improve computer modeling and simulations of the potential USHPRR fuels by providing raw data as well as rudimentary correlations between fission density and porosity. Ultimately, the goal is to provide microstructure data to modelers that are statistically valid, along with creating a method for this analysis to be used in future experiments.

2. BACKGROUND

2.1 RERTR-12 and AFIP6-MkII history

RERTR-12 and AFIP6-MkII are two irradiation experiments created to explore the behavior of U-Mo alloy fuel under intense irradiation conditions. Though the material and goals were similar, samples produced for each experiment were quite different [8]. AFIP6-MkII experiments consisted of two full-sized plates, and RERTR-12 consisted of 56 mini-plates fabricated in a slightly different way to the AFIP6-MkII plates. Both RERTR-12 and AFIP6-MkII were irradiated face on in ATR [7 -9]. While there are many dissimilarities between RERTR-12 and AFIP6-MkII, the most concerning is the difference in swelling behavior. AFIP6-MkII exhibited more drastic swelling measured during the post-irradiation examination (PIE) than RERTR-12 [9, 10].

The differences in the starting microstructure, highlighted in past work, were hypothesized to be the cause of the observed swelling behavior [11-13]. Both experiments' material was very heterogeneous. The heterogeneity accounts for some discrepancies seen in the various studies of microstructural data [11]. FGB growth and grain refinement affect fuel swelling behavior and are likely influenced by the starting microstructure [14]. These factors were therefore studied to see if they were the causes of the performance differences. But, the post-irradiation microstructure of RERTR-12 and AFIP6-MkII exhibited significant differences in porosity and pore size at similar fission densities that do not match the discrepancies in the swelling behavior of the two experiments [11]. From a DART [15] analysis of AFIP6-MkII and RERTR-12, the volume fraction of chemical banding and phase decomposition present in the as-fabricated fuel and the calculated fission density were used to predict the fuel volume increase due to swelling. From the results, AFIP6-MkII was predicted to have higher swelling due to the early onset of grain refinement observed in the material caused by the starting microstructure [14]. However, the three different AFIP6-MkII cross-sections exhibited different amounts of swelling. As Robinson et al. explained, if the starting microstructure were the sole determining factor of the swelling behavior, each of the three cross-section samples of AFIP6-MkII would have behaved the same way. [14]. Therefore, the starting microstructure may not influence fuel behavior during irradiation as much as expected. Further data collection and analysis are necessary to understand possible connections between the starting microstructure, irradiation conditions, and final behavior of metallic fuels.

2.2 Modeling and simulation data needs

Understanding the irradiation behavior of new fuels is critical to developing a useable product for reactor conversion. Microstructural behavior determines the mechanical behavior of materials during irradiation. Therefore, fuel microstructure must be well recorded and analyzed to understand the relationship between macro- and microscopic behavior. Recognizing these relationships can make the fuels more reliable and reproducible for implementation in the reactor.

Modeling and simulation of the behavior of materials during irradiation is a critical component of the M^3 objectives. Accurate modeling reduces the need for experimental work and increases the understanding of the physics and kinetics of materials during irradiation. Accurate models decrease the time, effort, and cost in the development of new and historic fuel types.

When no data is available, models and correlations are used in their stead. As more data becomes available, these correlations can either be proved correct, improved upon, or discovered to be inaccurate [2].

Nine microstructural modeling (MM) objectives were identified as necessary experimental data that are currently unavailable or lacking in detail. Below are the nine objectives and the microscopy techniques used to retrieve the data. All the information must be recorded with respect to what fission density each sample is exposed as well as temperatures and as-fabricated conditions.

Microstructure modeling needs:

1. Volume fraction of different phases pre- and post-irradiation
    a. Volume fraction of phase decomposition
    b. Homogeneity or banding present
2. Defects (dislocation, grain boundary, carbides, etc.) type, size, and density
    a. Grain boundary aspect ratio and size
    b. Volume fraction of grain refinement
    c. Dislocation density – focused on decomposed regions in the fuel meat, diffusion barrier, and cladding
    d. Carbide volume fraction
    e. Pore size distribution
3. Mo concentration and inhomogeneity (chemical banding)
4. Grain boundary bubble size and distribution as function of burnup
5. U-10Mo grain refinement volume fraction as fraction of burnup
6. Gas density of FGB
7. Defect diffusion (self-diffusion and Xe diffusion)
8. Grain boundary denuded zone width
    a. Thickness of region around grain boundaries with no FGB
    b. Variation with irradiation condition
9. U-Mo/Zr interdiffusion region
    a. Characterize phases
    b. Mo concentration profile
    c. Gas bubble density

While the MM objectives cover a wide range of microstructural features, this work will focus on microstructural features causing or enhancing more complex mechanical behavior. These underlying features are grain size (MM-2), phase decomposition (MM-1, 2), grain refinement (MM-2, 5), porosity (MM-2), and homogeneity of the fuel meat (MM-1, 2, and 3).

To achieve the above MM objectives, optical and SEM images were taken of the RERTR-12 and AFIP6-MkII samples and analyzed. This most recent analysis is focused on the porosity of these samples; additionally, grain size, decomposition, homogeneity, and grain refinement were obtained through this current analysis along with previous image analysis. The data collected were analyzed to find correlations between fission density and the microstructural features.

2.3 Importance of microstructure on fuel behavior

The microstructural behavior of each feature of interest - grain size, phase decomposition, grain refinement, porosity, and homogeneity of the fuel meat – is dependent on each of the other features. For example the as-fabricated grain size will impact the phase decomposition [16], grain refinement, and gas bubble formation, thus increasing the amount and rate of swelling [17]. Areas of low molybdenum content in the starting microstructure increase the volume fraction of phase decomposition and consequently encourage grain refinement to occur at lower fission densities [18]. Therefore, the material's homogeneity can predict the onset of grain refinement through decomposed areas. All this to say each microstructural feature must be understood to better predict and model more complex systems, such as fuel swelling, of the material properties.

2.3.1 Decomposition

Decomposition of the stable γ uranium phase to the less stable α uranium and γ' U_2Mo phase occurs during the fabrication process in U-Mo alloy fuels, and must be elucidated prior to irradiation [16]. The presence of the orthorhombic α phase enhances the rate and amount of swelling. During irradiation α uranium will change into γ, leading to smaller grains, therefore earlier grain refinement that will be discussed shortly [19]. Also, phase decomposition can lead to anisotropic swelling due to the loss of the stable γ phase to the anisotropic phase, leading to tearing at grain boundaries and swelling [19]. To mitigate the amount of phase decomposition a homogenous material with large grains is desirable. The larger the grains the less area for nucleation of the α + γ' phase to occur [14, 18]. Therefore, the starting decomposition volume fraction and grain size is important to modeling and understanding the swelling behavior of a material.

2.3.2 Homogeneity

Chemical banding or homogeneity of the constituents impacts the development of FGB, grain refinement, and ultimately the swelling. Areas with low molybdenum content along grain boundaries lead to the phase decomposition previously discussed. It will also cause grain refinement to start at a lower fission density [21]. As the amount of molybdenum decreases, the grain boundary energy increases with increasing temperature. Interfacial energies of BCC molybdenum are much higher than uranium, and this difference causes the molybdenum depletion at the grain boundary. At high temperatures this energy difference between uranium and molybdenum lessen. Therefore, the chemical constituents are more homogenized. Higher annealing temperatures allow for a more homogenous material with larger grain boundaries to prevent phase decomposition, and ultimately swelling [21], [22]. If a material is more homogeneous, the amount of phase decomposition can be controlled. So the grain refinement resulting from the smaller α grains can be better controlled and help prevent swelling [19].

2.3.3 Fission gas bubbles and grain refinement

Swelling in nuclear fuels is primarily due to the fission gases produced during irradiation [6]. These gases form bubbles along grain boundaries (intergranular) and inside the grains

(intragranular). Intergranular FGB contribute significantly more to the swelling than the intragranular bubbles. This is because nanobubbles that form along the grain boundaries can combine more easily to become much larger bubbles [19]. Swelling due to this gas formation occurs at low fission densities, where the typical size of a FGB is about 3.5 nm [23]. Gas bubbles first form an FCC lattice structure (the fission gas superlattice) and are reasonably stable at fissions densities under $4x10^{21}$ fissions/cm^3 (f/cm^3) [14, 15, 17, 18].

Grain refinement is an essential factor in predicting the swelling of monolithic fuels and is dependent on the phase decomposition, homogeneity, and starting grain size as mentioned in the previous sections. Refined grains are grains that have been subdivided into smaller grains during irradiation. Therefore, more grain boundaries are created allowing for more fission gas swelling to occur at the grain boundaries by destroying the fission gas superlattice. The destruction of the superlattice transforms small, high-density intragranular bubbles into large (~3.5 nm), low density intergranular bubbles [24]. Because of these phenomena, grain refinement can increase swelling to approximately 5.9% [24].

Grain refinement is highly dependent on fission density. It begins at fission densities around $3x10^{21}$ to 5 $x10^{21}$ f/cm^3 and prominently impacts the gas swelling between fission densities of $2.5x10^{21}$ and $3.5x10^{21}$ f/cm^3 [14, 15, 17, 18]. However, there is a limit to how much grain subdivision may occur in the material. Post-recrystallized grains found in U-Mo dispersion fuels irradiated to $6.3x10^{21}$ f/cm^3 were similar to those seen in monolithic U-Mo samples irradiated to the much higher fission densities [19, 20]. The similarities of the structures indicate at fission densities above $6.3x10^{21}$ f/cm^3 grains do not continue subdividing [27].

2.3.4 Porosity

During PIE, FGB are studied by measuring the pores left in the microstructure. The size and volume of the pores are an artifact of the size and volume of the FGB. The attributes of these microstructural pores can be studied in reference to the fission density to understand the behavior of the FGB as a function of fission density. These pores also indicate the effects FGB have on other microstructural behaviors. At high local fission densities (~$9.8x10^{21}$ f/cm^3), transmission electron microscope (TEM) characterizations showed monolithic U-Mo alloy fuels exhibit relatively large, possibly interconnected bubbles with diameters larger than 1 μm and solid fission product precipitates in those bubbles. However, small bubbles (<200 nm) were also prevalent. These foil samples showed that at high fission densities, U-Mo monolithic fuel can exhibit swelling of ~76% [27]. Focused ion beam (FIB) TEM investigations of monolithic U-Mo fuels uncovered the presence of small, 2 nm-sized intragranular bubbles [27]. Previously, it was thought that large FGB govern the microstructure, and small bubbles are less influential at high fission densities (>$7x10^{21}$f/cm^3). However, these samples were irradiated to the high fission densities. A high concentration of smaller bubbles implies these bubbles inhibit grains from swelling by maintaining the high gas inventory inside the smaller, dense bubbles [27]. The large population of small gas bubbles at a high fission density suggests there is something other than fission density determining the evolution of the various sized bubbles in the material [27]. Quantifying the development of FGB is necessary to understanding swelling in metallic fuels and is why this study focuses on the FGP present in the AFIP6-MkII and RERTR-12 experiments.

3. HISTORIC RERTR-12 AND AFIP6-MKII DATA

3.1 Fuel fabrication

Both AFIP6-MkII and RERTR-12 experiments utilized U-10wt%Mo for the fuel matrix and a zirconium diffusion barrier applied by co-rolling the assemblies. Following this, the samples were hot rolled, annealed, and cold rolled to the proper thicknesses. Table 1 below highlights the differences of fabrication methods of the samples. The most noticeable difference shown is in the number of passes completed during the cold-rolling process [7-9]. The cold-rolling schedule of AFIP6-MkII was more gradual (40% reduction during 44 passes) than RERTR-12 (20% in only four passes)[9, 12]. The other notable difference in fabrication techniques is the hot-isostatic pressing (HIP) ramp rates [8]. The ramp rate used in the HIP treatment of each sample causes the differences in phase decomposition observed. RERTR-12 samples were produced with a much faster heating and cooling rate as well. This treatment prevented a very high amount of phase decomposition from occurring compared with AFIP6-MkII [11]. In addition to the fabrication differences, RERTR-12 samples contained uranium with 70% ^{235}U enrichment, and AFIP6-MkII contained 40% ^{235}U [11].

3.2 Characterized samples

As previously stated, it is vital to understand the beginning and post-irradiation microstructure of a material. Past analyses of two archival samples of the RERTR-12 (JJ1031) and AFIP6-MkII (CB1131) are presented in Table 2 through Table 5 and show some of the samples' starting microstructural features. Phase decomposition, carbide volume fraction, grain size, and Mo banding were all explored in past work [9, 13]. The most drastic difference in the two samples is between the amount of chemical banding and the phase decomposition. As stated previously, each of these can impact fuel performance during irradiation. Phase reversion of α to γ during irradiation has been hypothesized to lead to smaller grains in the material or residual dislocation networks. Therefore, the α phase could lead to more grain refinement or cause it to happen sooner during irradiation and subsequently cause higher swelling [14]. Chemical banding is caused by the inhomogeneity of the elemental concentration of the two as-cast alloys that were then rolled as foils to fabricate the monolithic fuel plate. Higher amounts of decomposed regions and inconsistent grain sizes result from this inhomogeneity [16, 23]. SEM images were analyzed using the ASTM-E562-11 standard [29] to measure the volume fraction of the Mo content across the sample images. From this point count method, the volume fraction of banding in AFIP6-MkII was 100%, and RERTR-12 exhibited banding in ~88% of the matrix [14]. These values indicate the concentration of Mo is not uniform throughout most of the matrix. Examples of the phase decomposition and banding present in the as-fabricated samples of RERTR-12 and AFIP6-MkII are shown in Figure 1 and Figure 2 [14]. The very dark regions seen in the figures are the decomposed α phases, and the lighter areas across the image are areas of low molybdenum content. The values of the characterized archival samples' banding and decomposition are in Table 2.

Table 1. Differences in benchmark as-fabricated samples of RERTR-12 and AFIP-6MkII (red text highlights differences) [8]

	JJ1031 (Alloy 328-2, RERTR-12, plate ID L1P757, HIP 58-4)	CB1131-F8 (Alloy342-1-1, AFIP-6MKII, plate ID UM0-342-1-1)
Feed stock	INL HEU	Y–12 HEU (coupon 3G60-C7-PA24)
Casting	INL arc melting	Y–12, vacuum casting, no in-mold annealing
Enrichment	70%	40%
Foil thickness, including Zr (mil)	12	14.9
Hot rolling passes	9	12
Max hot rolling reduction (%)	40	20
Total hot rolling reduction (%)	85	84
Total hot rolling time at 650°C	80 min	80 min
Post hot rolling annealing at 650°C	45 min	45 min
Cold rolling passes	4 (aggressive)	44
Total cold rolling reduction (%)	20	40
Flattening at 650°C /1hour	No	No
Total time at 650°C	125 min	125 min
Foil characteristic	Wavy (after cold rolling)	Flat (after cold rolling)
HIP run temperature (°C)	560	560
HIP run pressure (psi)	15000	15000
HIP run ramp rate (°C/hour)	280	Used a slower ramp rate
HIP bonding time at 560°C (minutes)	90	95
HIP run variables	Six plates per HIP can	Two plates per HIP pack, thicker cladding, without top strong-back
Note	Mini-plate benchmark, RERTR-12 first insertion, Carbon less than 400ppm	Carbon 692ppm, Iron 80ppm,

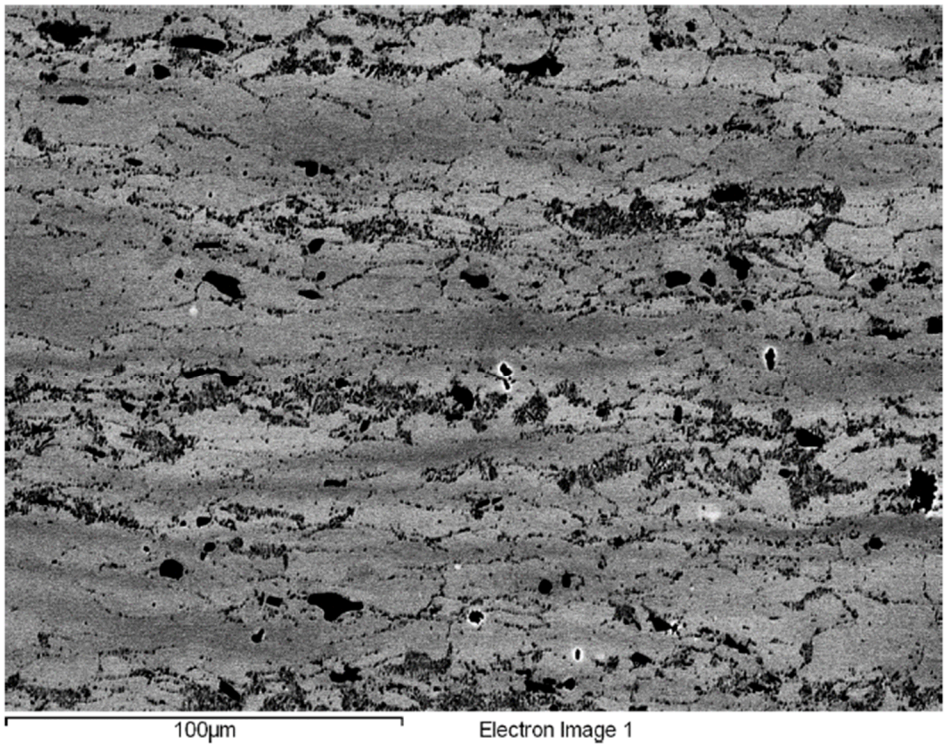

Figure 1. Backscatted electron micrograph showing decomposition and banding in the U-10Mo foil for the AFIP6-MkII archival sample [14]

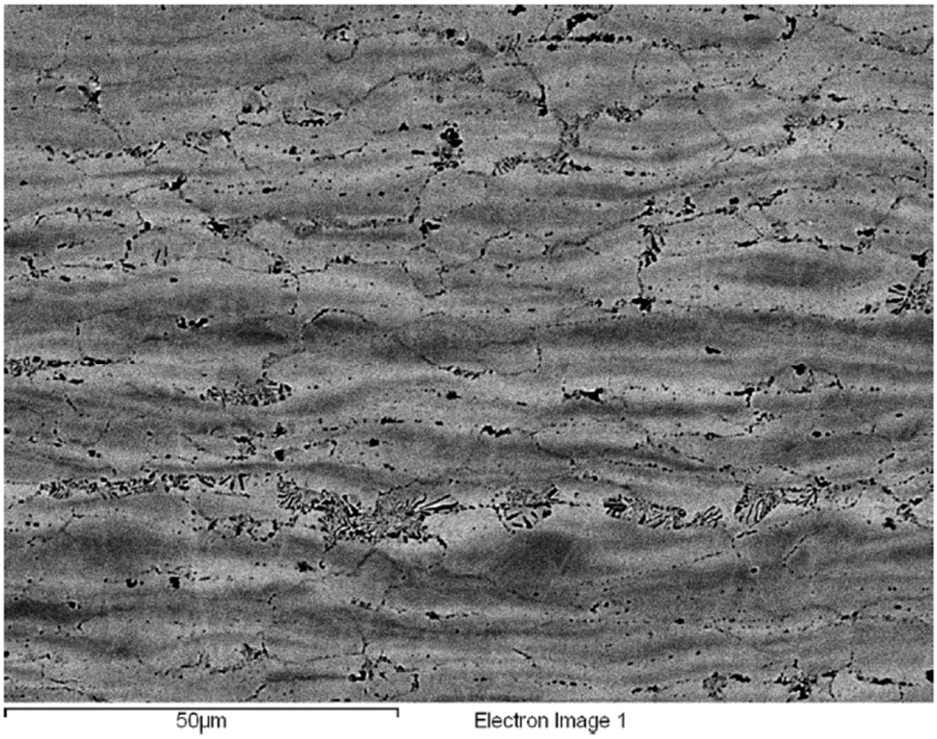

Figure 2. Backscatted electron micrograph showing decomposition and banding in the U-10Mo foil for the RERTR-12 archival sample [14]

Table 2. Banding and decomposition volume fraction values of RERTR-12 and AFIP6-MkII as-fabricated samples [14]

Sample	Banding (%)	Decomposition phase (%)
RERTR	100	7.4±3.6
AFIP6	~88	18.0±6.1

Table 3 presents another set of data from the archival, as-fabricated samples. The magnification of 500X was determined to be the more representative of the sample material than SEM images at higher magnifications. The higher magnifications at the same positions showed localized effects rather than a representative sample of the whole microstructure, and were therefore not included in this analysis [11]. Light and dark phases are a measure of the chemical banding observed [11]. The results of phase decomposition are slightly different from the previously reported values, probably because of the difference in image analysis techniques used. For completeness, the average grain size and carbide volume fraction are included.

Table 3. Past SEM image analysis of historical as-fabricated samples [11]

Sample	Magnification	Light phase (%)	Dark phase (%)	Decomposition phase (%)	Carbide volume fraction (%)	Mean grain area (μm^2)
RERTR-12 (JJ1031)	500X	59.00	41.00	7.63	2.44	54.13
AFIP6-MkII (CB1131)	500X	60.17	39.83	14.18	3.95	68

3.3 Early PIE of samples

In Table 4 and Table 5 are results from previously analyzed PIE images of irradiated AFIP6-MkII and RERTR-12 samples. The discrepancies between the datasets are again due to the differences in image analysis, image quality, and where the images are from on the sample [9, 13]. From Table 4 the expectation is AFIP6-MkII will exhibit similar porosity as RERTR-12 from the top plate, but have much higher values at the middle and the bottom plate [14]. However, in a separate analysis (Table 5), the expectation is that the samples will have similar porosity [11]. The un-recrystallized portions also do not agree. Extremely low values of the non-recrystallized area in Table 5 at the higher magnifications are possibly due to the minimal area the image encapsulates. The material is heterogeneous, and these may be localized values rather than a representation of all the microstructure [11].

Table 4. Summarized data from past work on AFIP6-MkII and RERTR-12 [14]

Sample ID	Fission Density	Carbide precipitates (%)	Unrefined grain regions (%)		Porosity (%)
				Sub-routine excluded	
AFIP–6 MkII Top	4.53E+21	1.0	22.3	13.8	11.8
AFIP–6 MkII Middle	4.85E+21	0.9	11.4	6.9	16.5
AFIP–6 MkII Bottom	4.90E+21	0.8	2.8	1.6	27.2
L1P755	4.67E+21	0.0	10.6	4.7	13.3
L1P773	3.35E+21	0.0	25.1	15.2	13.7

Table 5. SEM image analysis results of irradiated RERTR-12 and AFIP6-MkII[11]

Sample	Mag	FD(10^{21} f/cm^3)	Porosity (%)	Mean pore area (μm^2)	Mean pore diameter (μm)	Grain size diameter (μm)	Unrefined grain regions (%)	Mean un-recrystallized area (μm^2)	Carbide vol frac (%)
L1P755 (KGT2055)	500X	5.2	17.88	2.66	1.67	N/A	0.21	14.72	N/A
L1P755 (KGT2055)	5000X	5.2	20.72	0.12	1.83	8.57	5.11	0.31	N/A
AFIP6 KGT2144	500X	5.1	20.74	3.13	0.34	N/A	1.32	13.89	N/A
KGT2144	5000X	5.1	21.22	0.20	0.42	7.43	16.42	0.55	1.43

PIE nondestructive analysis used profilometry to measure the thickness of the fuel plate to examine the amount of local swelling. Swelling in metallic fuels is often highest near the edges of the fuel plates [25,26]. AFIP6-MkII and RERTR-12 are no exception. When analyzing the microstructural characteristics of the fuel at regions near the edges these differences in swelling behavior and applied stresses are important to consider. If the swelling is due to only fission gas products, larger pores are expected at the areas of high swelling. However, irradiation-assisted creep at high fission densities has been hypothesized to also create the uneven swelling observed in AFIP6-MkII and RERTR-12 from cladding constraints [11, 25]. Compressive and tensile stresses between the cladding and the fuel swelling near the foil edges will also impact the microstructure at these areas. Effects of the cladding constraints and decreased swelling on the microstructure are considered in the analysis presented later in this report.

4. STANDARDIZED CHARACTERIZATION TECHNIQUE

4.1 AFIP6-MkII and RERTR-12 fuel plate samples

From the AFIP6-MkII experiment only one plate was irradiated due to a failure of a section of the fuel assembly during irradiation [13]. Of that plate, different sections were cut and used for various materials testing. Figure 3(a) shows the different sections and highlights the application for each. Three, 2.54 cm by 0.02 cm U-Mo mini-plates were cut from the larger plate and are shown in orange on the diagram as the top, middle, and bottom sections. An enlarged view of the transverse cross-section of each miniplate is shown in Figure 3 parts (b), (c), and (d). Calculated fission densities are presented along the cross-section images at their corresponding test locations. The top sample (95A, now KGT2763) was cut into a length of 0.953 cm due to sample preparation problems [32]. A shorter sample may impact the results found in the analysis. Cutting the sample may change the microstructure, or the analysis may be biased by reducing the sample area compared to the other two sections. However, for completeness the sample was analyzed and included in this report. After further exploration the sample may be determined to be an unreliable sample to inform the dataset, but the sample was not ruled as unacceptable in this early analysis. The middle plate (96A) and bottom plate (97A) remained the same 2.54 cm length.

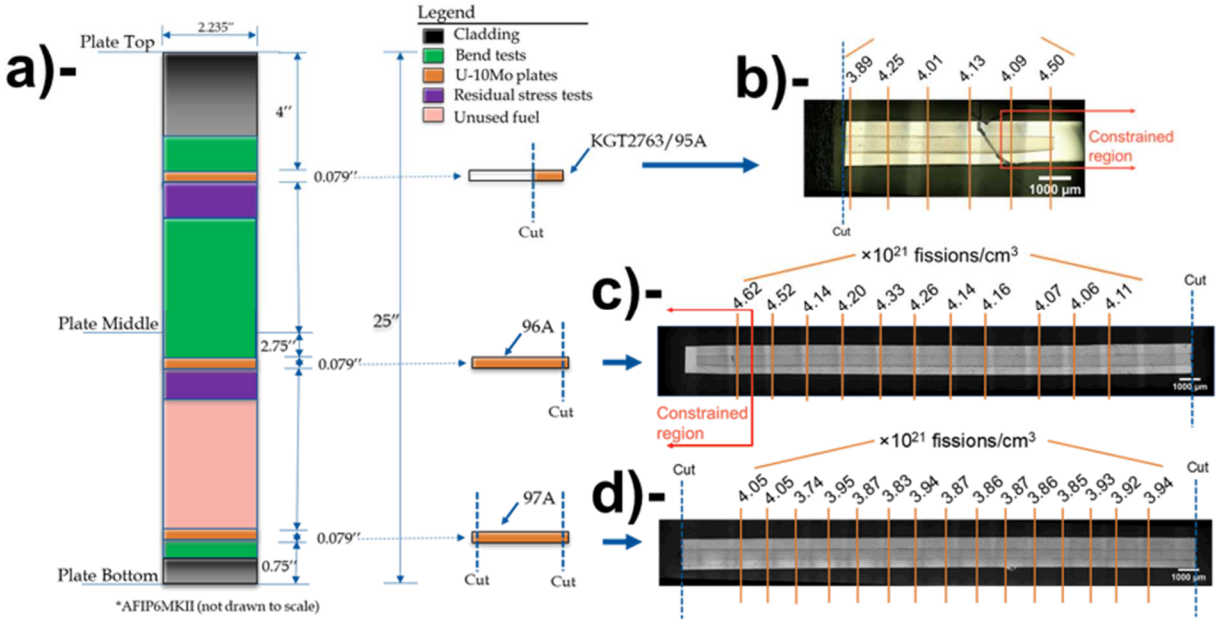

Figure 3. AFIP6MKII full-sized plate illustrating the dimensions of the sample mini-plates cut from the top, middle, and bottom plate.

At the edges of samples KGT2763 and 96A are rail regions where the aluminum cladding restricts, or constrains, the behavior of the fuel. As stated previously, swelling measurements of both AFIP-6 MkII and RERTR-12 samples showed a notable decrease at the fuel edges. Additionally, the interaction layer (IL) of the zirconium diffusion barrier and fuel meat does not increase with the fission density as expected in these regions. To estimate the area of the samples affected by cladding constraints, the IL was measured across the transverse section of 96A. Near the foil's edge the IL thickness decreases significantly. The distance from the foil's edge to the

decreased IL thickness is ~1.5 mm in AFIP6-MkII and ~1 mm in the RERTR-12 sample and is the area most constrained by the cladding. Figure 4 illustrates where these constrained regions are along the plate and sample foils.

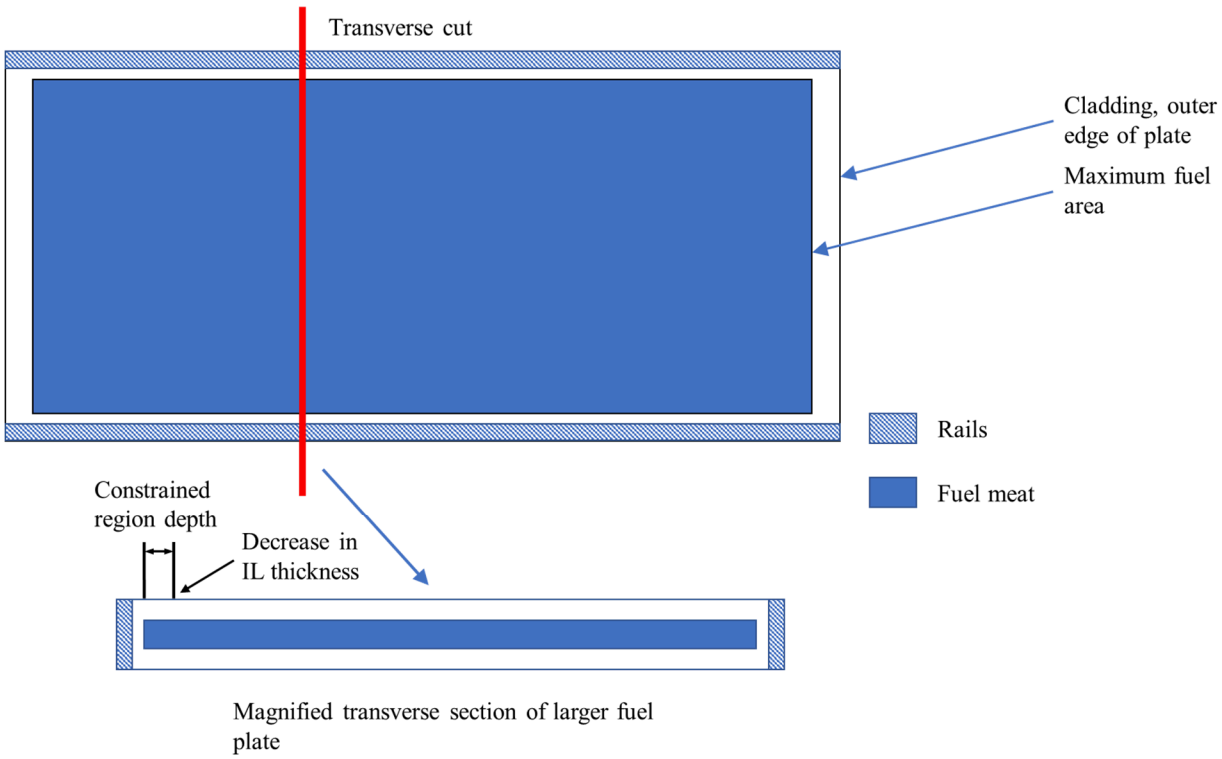

Figure 4. Rail region diagram of full plate and transverse cut sample

Identifying the rail regions is important when analyzing the microstructural results. Data from these regions may not be representative of the actual fuel behavior due to the restricted swelling observed at these points from non-uniform compressive stress on the plate. 97A was cut such that there were no rail regions present on the sample, shown in Figure 3(d).

The RERTR-12 sample, L1P755, was irradiated similarly to AFIP6-MkII, face on to the ATR core. L1P755 is a sister to the archival sample, L1P757 (met mount JJ1031) [8]. This allows for the direct comparison of pre- and post-irradiated samples to understand possible connections between the two microstructures. Figure 5 is an image of the transverse cross-section of L1P755 with the fission densities at each location clearly labeled. On both sides of the sample are rail regions. Three test locations on the right are in this rail region, while one test location borders the rail region on the left, leaving five test location unimpacted by the rail regions. L1P755 had a much higher range of fission densities compared to the samples of AFIP6-MkII, making direct comparisons of the two datasets' microstructure difficult.

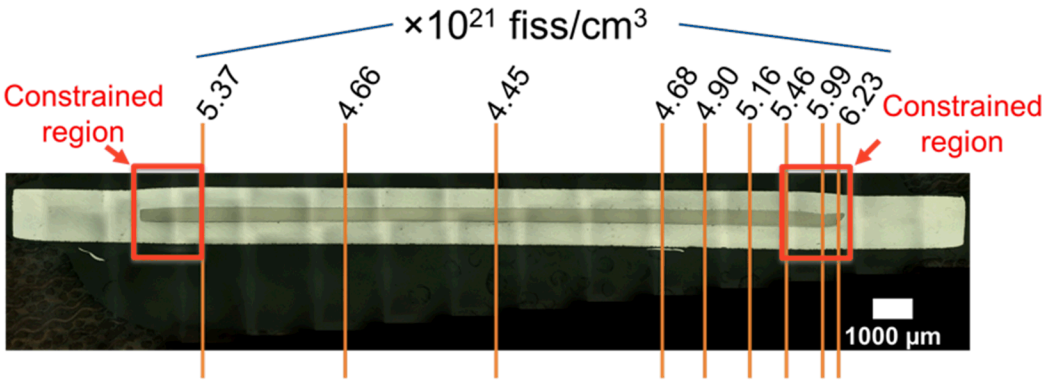

Figure 5. Optical micrograph showing the transverse cross-section of L1P755 and the associated fission density for the different test locations

4.2 Image analysis

Image J, ASTME562 standard [33], and the automated fission gas pore graphical user interface (FGP-GUI) [34] characterized the miniplate microstructure. The FGP-GUI determined the pore size and morphology, along with the average porosity, pore area, diameter, and eccentricity. ASTME562 standard verified the FGP-GUI and ImageJ porosity results and estimated the area fraction of un-recrystallized material. The standard determined the thickness of the fuel cladding chemical interaction layer as well. RERTR-12 and AFIP7 samples analyzed with this method verified the use of the FGP-GUI developed at the University of Florida as a viable method of automating and standardizing image analysis [7].

Backscattered electron (BSE) micrographs were taken of the fission gas pores (FGP) at the various fission densities across each sample. Figure 6-Figure 9 show example micrographs of the pore evolution in each sample with the corresponding fission density (x10^{21} f/cm^3) displayed in the corner of each. The images are presented in order of their location on each sample (as shown in Figure 5) starting at the left side of the plate and moving right. Each sample inside the rail region is labeled. Highlighting the porosity images in the rail regions allows for the comparison of microstructures affected and unaffected by the cladding constraints. Figure 6 highlights examples of solid fission products, FGPs, and grains as well.

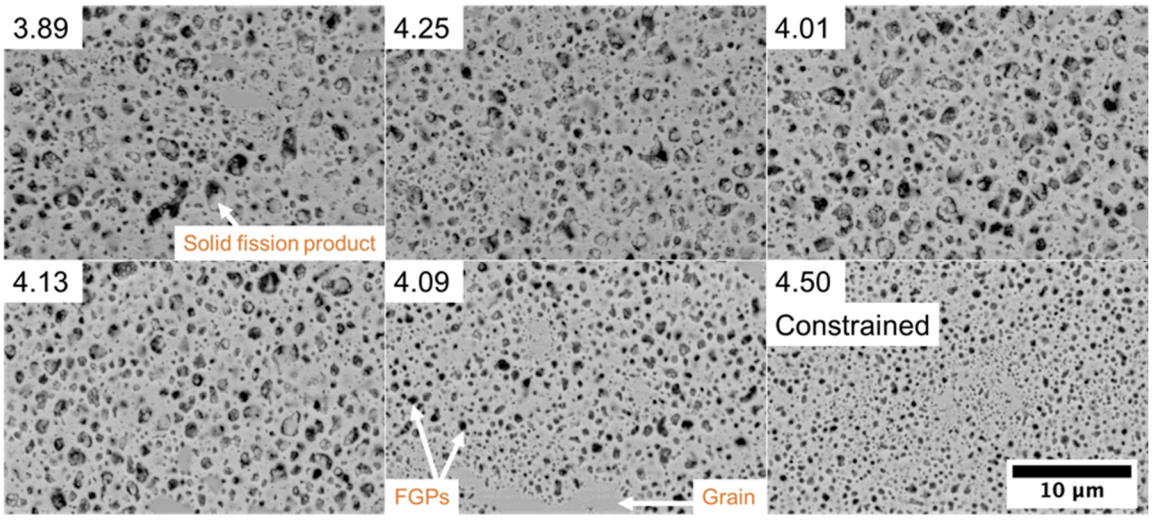

Figure 6. Representative BSE micrographs of KGT2763 demonstrating the fission gas pore distribution at different calculated fission densities in units of $\times 10^{21}$ fissions/cm^3

In the constrained region of KGT2763 (Figure 6), the suppressed swelling is visible when compared to the other images in the non-rail areas. The pores appear much smaller than the other non-restrained areas, as shown in Figure 6 at the fission density 4.50x10^{21}f/cm^3. However, the difference in the calculated fission densities of each image location is small. Due to uncertainties in this calculation method it may be assumed there is not as significant a difference in the highest fission density and the lowest of this sample. Future work will quantify these errors, or uncertainties. Solid fission products are also visible in the micrographs of KGT2763 in all but the rail regions.

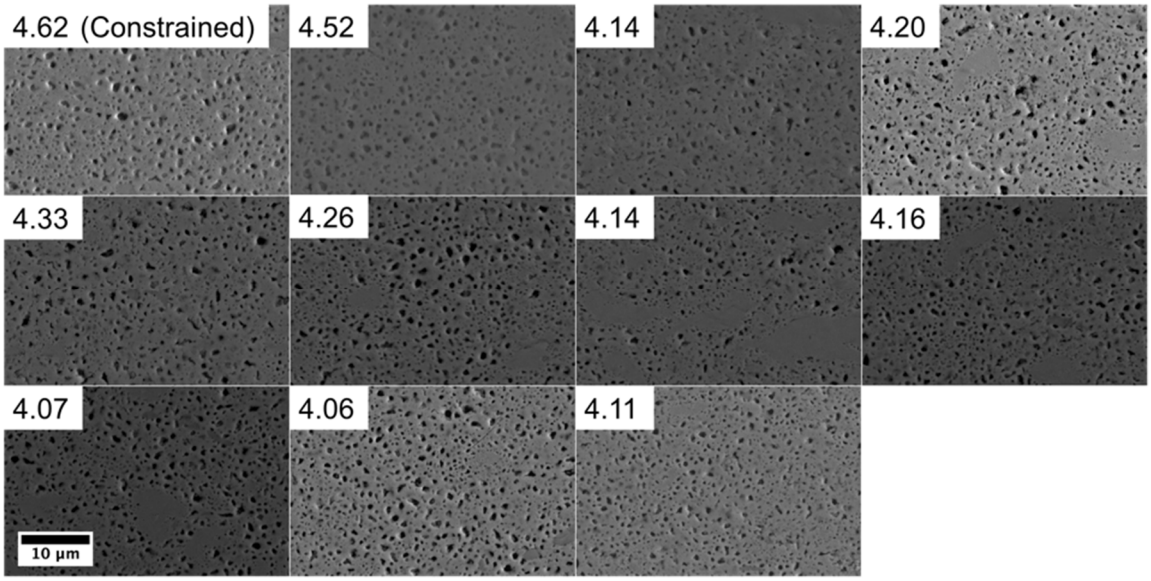

Figure 7. Representative BSE micrographs of 96A demonstrating the fission gas pore distribution at different calculated fission densities in units of $\times 10^{21}$ fissions/cm^3

Figure 7 shows the micrographs of sample 96A, or the middle section of AFIP6-MkII. The overall fission density of this sample is higher than those of KGT2763. Visually, the pores

appear smaller than in KGT2763 as well. The rail region in 96A, however, does not appear to have the constrained pore growth like that seen in the previous sample even though it also has a higher fission density. The consistent pore size across 96A may show there is a difference in the stresses applied by the cladding down the length of the plate between the top and middle. For example, the cladding may be constraining the top section more than the middle, thus creating the smaller pores.

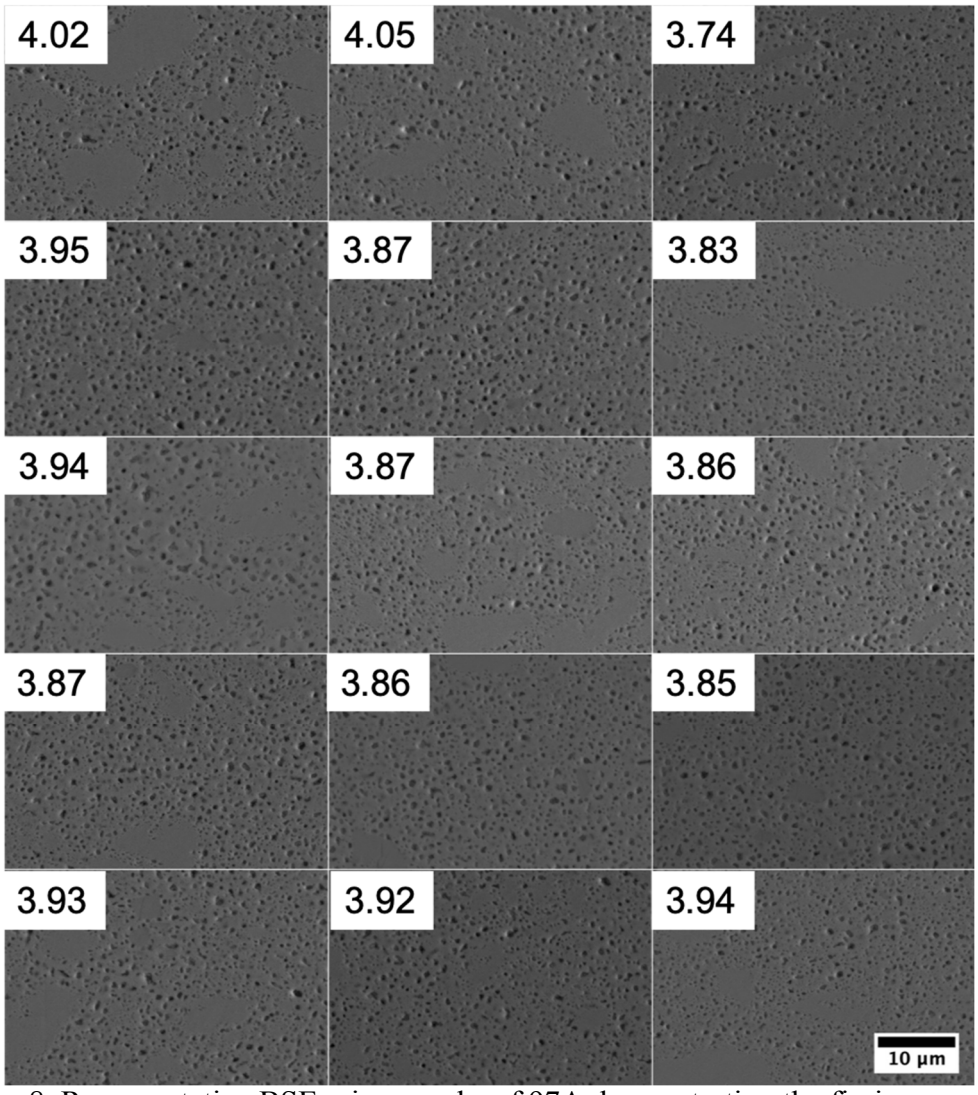

Figure 8. Representative BSE micrographs of 97A demonstrating the fission gas pore distribution at different calculated fission densities in units of $\times 10^{21}$ fissions/cm^3

The fission densities calculated for sample 97A (Figure 8), or for the bottom of AFIP6-MkII, are the lowest on average of the three samples. Pores appear evenly distributed, and each micrograph shows areas of unrefined grains. 97A does not contain any rail regions, and therefore is the most uniform of the three samples.

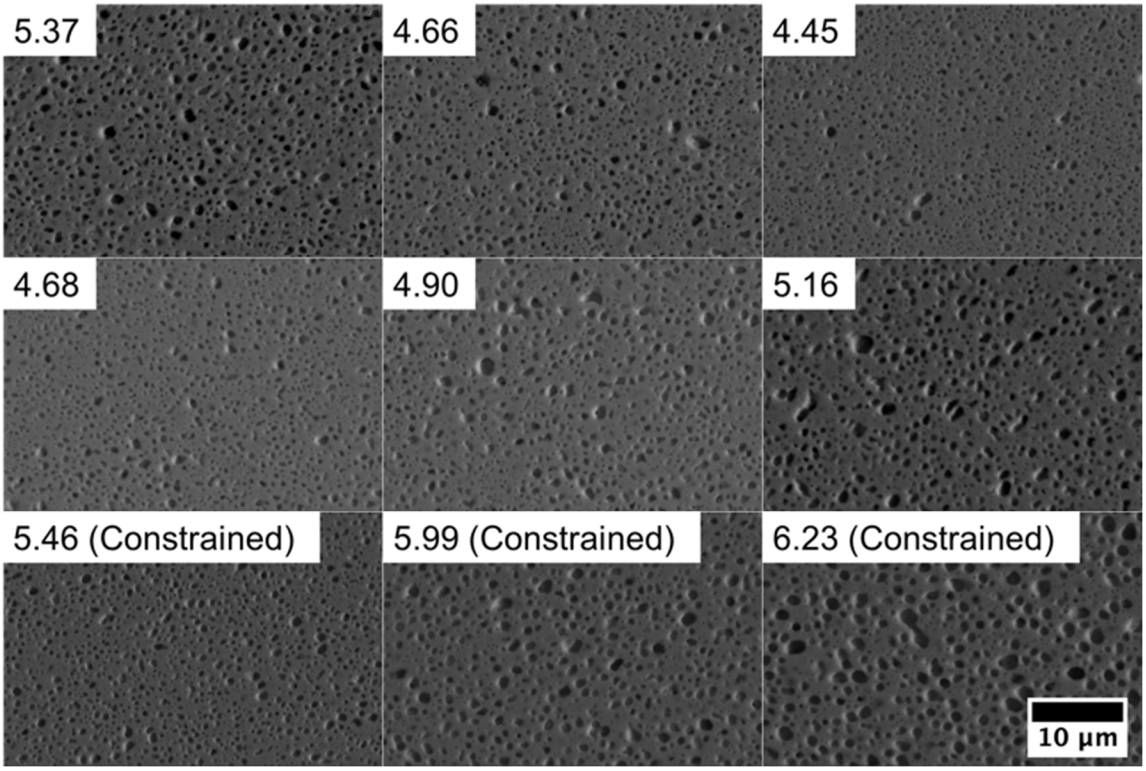

Figure 9. Representative BSE micrographs of L1P755 demonstrating the fission gas pore distribution at different calculated fission densities in units of $\times 10^{21}$ fissions/cm^3

Unlike the AFIP6-MkII micrographs, all the grains in the L1P755 micrographs (Figure 9) are recrystallized due to the higher fission densities. The lowest fission density is 4.45×10^{21} f/cm^3. The higher fission densities of RERTR-12 also caused larger FGP formation. In contrast with KGT2763 and 96A, the pores in the rail regions appear to respond differently. At the far left of the sample the fission density of 5.37×10^{21} f/cm^3, the pores are very similar to those in the non-rail regions. The location of this micrograph is on the very edge of the rail region and therefore may not exhibit very different microstructure as compared to other regions. The last three locations measured at the right of the sample have increasing pore size. The region exposed to a fission density of 5.46×10^{21} f/cm^3 has smaller pores compared to the other rail regions and non-rail regions. Moving further to the end of the sample, at 5.99×10^{21} f/cm^3, the pores increase in size and are comparable to those in the center of the sample. The point farthest down the sample has the largest pores, which is opposite of the small, restricted pores that are expected to develop under the constraints of the cladding in the rail region. Further investigation is required to identify the influences of these rail regions on the FGP and why it appears inconsistent between the two AFIP6-MkII samples and L1P755.

4.3 Data analysis methods

Four aspects of the microstructural FGPs are presented here for the AFIP6-MkII and RERTR-12 experiments: the porosity, pore diameter, pore size area, and eccentricity. For this work, pore size area is defined as the cross-sectional area of each pore in the micrograph. Pore diameter is the average diameter of each pore used to determine the pore size area. And the

porosity is the fraction, or percent, of the entire micrograph area occupied by pores. The eccentricity is a measurement of the elongation, or how lamellar, the pores are. Data analysis in this report used various Python statistical packages along with the statistical software R [24, 25]. Each sample contains a different number of fission densities at the associated location on the sample that must be analyzed to understand the data. Microstructural modeling requires the use of simple data points and more complicated equations based on correlations. This work uses the pore size area data to develop a method of analyzing microstructural data for modeling purposes.

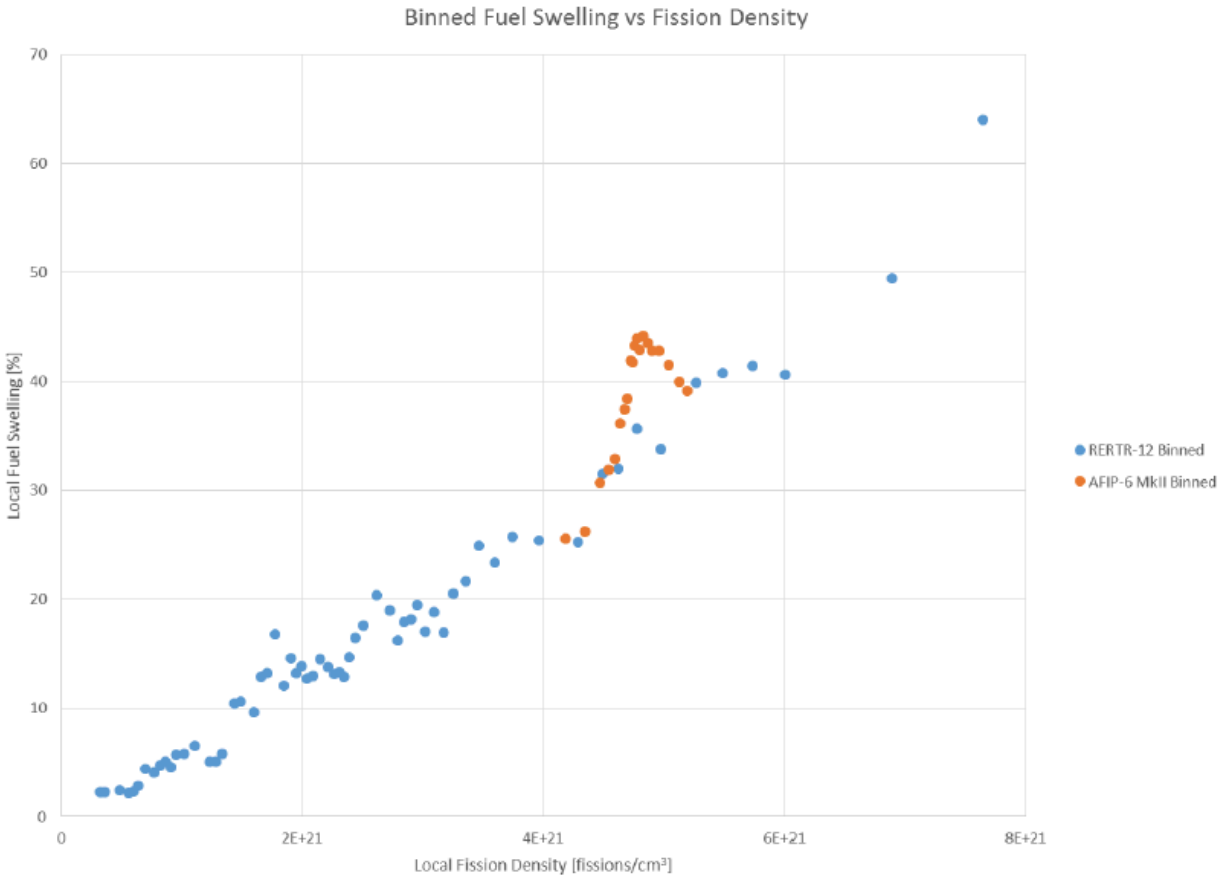

Figure 10. Fuel swelling based on local fission density in RERTR-12 and AFIP-6 MkII experiments [14]

As shown in Figure 10 the differences in the swelling behavior of the fuel plates from the AFIP6-MkII and RERTR-12 irradiations are quite different from each other. The actual swelling fractions may not be extremely different, but the differences in the swelling response to changing fission densities is curious. It is necessary to search the data for possible connections or relationships not apparent in the summary of the data to understand the different behaviors. The normality of each dataset is found using the null hypothesis that data has a normal distribution using the D'Agostino and Pearson's test. The normality of the data is an important aspect to ascertain because it determines what further statistical tests to implement. Following the tests of normality, descriptive statistics are calculated, i.e., mean, median, maximum values, and minimum values of the pore size area. Visual inspection of the data using box plots, histograms, and scatterplots allows for a better understanding of how the data is behaving over the various

fission densities and experiment samples. Data transformation tools are implemented to ensure the normality of the pore size area data for further analysis. ANOVA (analysis of variance) and ANCOVA (analysis of covariance) are used to explore any existing relationships between fission density and the post-irradiation microstructure. Linear relationships were explored for the entire dataset to determine if fission density alone is a useful predictor of pore size area. The methods employed in this data analysis are explained in greater detail in the discussion and results section.

5. RESULTS & DISCUSSION

5.1 Summarized data

Table s6 contains the average values and the associated standard deviation of the four pore features measured by the automated image analysis method at each sample. KGT2763 and L1P755 samples experienced the highest fission density and exhibit the highest average values of pore size area, pore diameter, and porosity. The values of KGT2763 are much larger than those of 96A and 97A, even though all three come from the same experiment. The pore size of KGT2763 is 44% higher than the closest value of 96A, with a ~37% higher porosity. It was expected 97A would have the smallest of all the pore sizes and porosity values due to the lower average fission density it experienced. From this brief look at the results, KGT2763 and L1P755 behaved similarly to each other despite the higher fission density of RERTR-12.

Table s6. Summary pore data of AFIP6-MkII and RERTR-12

Sample	Pore size area (μm^2)	Pore size area S.D.	Porosity (%)	Porosity S.D.	Pore diameter (μm)	Pore diameter S.D.	Eccentricity	Eccentricity S.D.	Average fission density (10^{21} f/cm^3)
KGT2763	0.27	0.06	24.24	3.11	0.47	0.08	0.63	0.03	4.14
96A	0.15	0.01	15.04	1.77	0.38	0.01	0.69	0.69	4.24
97A	0.12	0.01	15.49	1.18	0.35	0.01	0.64	0.02	3.91
L1P755	0.25	0.08	25	3.22	0.5	0.07	0.62	0.02	5.21

More detailed data results for each fission density are presented in Appendix A and B, including the average, minimum, maximum, quartile values, and standard deviation. Statistical analysis for pore size is included in Appendix A, and the analysis for porosity, eccentricity, and pore diameter are included in Appendix B. Using the averages presented in the appendices, Figure 11 shows the scatterplots of all AFIP6-MkII and RERTR-12 samples. To explore the relationship between the fission density and the microstructure characteristics, a regression line and the corresponding equation are also presented on the plots for each sample in Figure 11. If fission density is the only factor impacting the microstructural changes during irradiation a linear relationship between the two would be expected, e.g. as the fission density increases so will the pore size area. Both RERTR-12 and AFIP-6 MkII would have behaved in the same manner.

However, from this analysis, it is clear the two do not react similarly to the fission density increases. The goal of plotting the linear relationships was to elucidate any pore characteristics that appear to be closely correlated to fission density. If one pore characteristic were easily predicted with a known fission density it may be a starting point for finding other connections between fission density and microstructural evolution. The linear relationships between fission density and pore attributes proved to be very different for each sample. The R^2 value, indicating the strength of the linear relationship to the data, is low for all but L1P755. This suggests a non-linear relationship exists between fission density and the pore data. KGT2763 is the most dissimilar from the other three samples except when considering the pore diameter. This may be due to artifacts caused by cutting the KGT2763 sample, or due to the very small number of locations data are retrieved from for the sample. From the results, there is a negative relationship between fission density and pore size area, eccentricity, and porosity, opposite of the anticipated relationships.

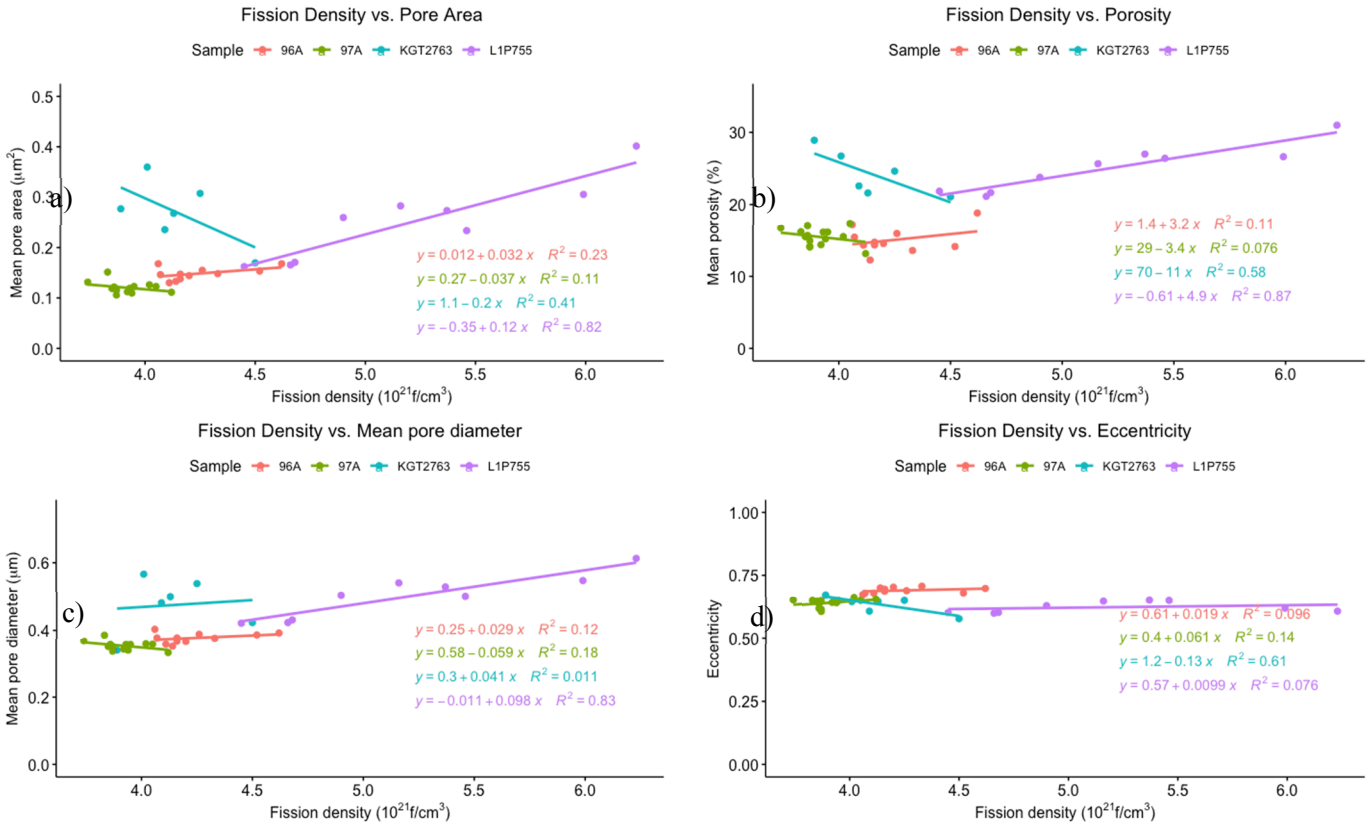

Figure 11. Scatterplots of pore information of RERTR-12 and AFIP6-MkII a) pore size area, b) porosity, c) pore diameter, d) eccentricity

5.1.1 Porosity

Porosity (Figure 11 (b)) was highest in KGT2763 and L1P755. These samples reached porosities of ~30%, whereas samples 96A and 97A measured porosities between 10 and 20%. The lowest porosity values of KGT2763 were seen in the rail regions. In the rail regions of L1P755 and 96A, the porosity was the highest. These are conflicting results and must be analyzed further. When comparing the porosity of this data and past reported data from AFIP6-MkII and RERTR-12, there are discrepancies. Porosity in this study was higher by up to 50%

than in previous AFIP6-MkII top samples analysis. Several factors can be responsible for the differences in results, such as the image analysis techniques used, the micrographs taken, and the sample preparation technique. Continued work will focus on understanding the differences in reported pore data from the two experiments. Understanding the differences in results can lead to a clearer picture of the data currently available to use for modeling purposes.

Materials with high porosity (percent of the total area occupied by pores) and a high concentration of small FGPs can resist swelling according to the theory of the fission gas bubble superlattice stability [26]. Materials with large FGPs in conjunction with low porosity exhibit swelling resistance. Samples susceptible to swelling often have large FGPs with high porosity. Because of the correlation of pore size and concentration to swelling behavior, it is essential to compare the results of pore size area to the porosity. Pore size area as a function of fission density is plotted above in Figure 11(a). Figure 12 reflects the experimental correlation between the pore area and porosity of the four plates. Assuming a linear relationship, the calculated R^2 coefficients suggest that porosity in 96A and L1P755 are moderately correlated to the pore area; however, in the case of KGT2763 the correlation is weak. We believe that the weak correlation could be due to the limitation of representative data points in KGT2763. It should be noted that we expect that the porosity will eventually normalize due to the saturation of the pores such that the initially identified linear relationship between the rate of change of porosity with pore area reaches an inflection point. The porosity will not increase with pore size indefinitely; therefore, the linear fit assumed in Figure 12 is a very rough approximation of the correlation between porosity and pore area. The morphological evolution of the pores is observed to be most dramatic in L1P755 because the pore size increased by at least double across the plate transverse cross-section. Moreover, the recorded mean porosity of 25% in L1P755 was the highest among the four plates. The evolutionary assessment of the porosity with the pore area across the plate transverse cross-section indicated that L1P755 exhibited the most dimensional instability. Furthermore, L1P755 experienced the highest fission densities of all four plates which supports the observation of higher porosity and pore size. Conversely, the evolution of the porosity with pore area was more conservative in 96A and 97A such that their plate porosities was <20% and their pore areas $<0.2\mu m^2$. Based on the observed changes in pore morphology, 96A and 97A exhibited more dimensional stability than L1P755 because of their lower porosity and pore size. As reiterated throughout this report, the sample area for KGT2763 is only a fraction of the transverse cross-section of its mother sample, 95A. As a result, the data summarized for KGT2763 is only representative of the small fraction of 95A and poses a limitation on the interpretation of the behavior of the mother sample. Nevertheless, image analysis performed on KGT2763 suggests that, like L1P755, dimensional instability is more prominent amongst its AFIP6-MkII counterparts. Although the mean porosity and pore area in KGT2763 was 3% lower and 7% higher than in L1P755, respectively, extensive changes in pore morphology was more notable in KGT2763 than in 96A and 97A.

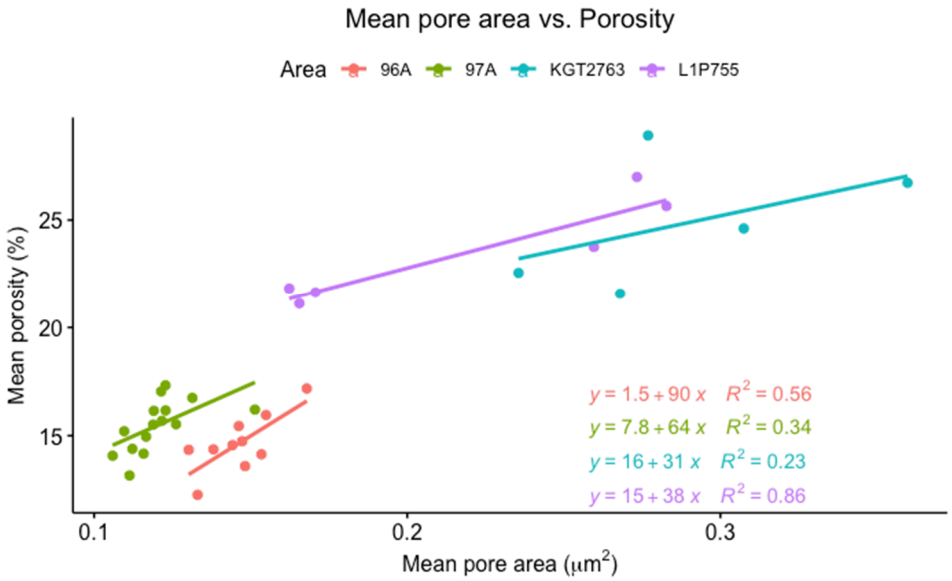

Figure 12. Pore area compared to mean porosity.

5.1.2 Eccentricity

Eccentricity, or the roundness of a pore, can tell a lot about the crystalline or amorphous nature of the FGPs [37]. Eccentricity values close to one imply a more crystalline FGPs and are favorable for stable behavior of a material [6]. As seen in Figure 11 (d), the eccentricity averages from the two experiments; all are between 0.50 and 0.75. Eccentricity behavior is the most similar characteristic of all the samples. Fission density does not appear to heavily influence the eccentricity as it increases, meaning the shape of the pores is not changing even if the number and size of the pores themselves are.

5.2 Pore size area data analysis

5.2.1 Boxplots

Boxplots visualize the data of each sample next to each other. Figure 13 shows a boxplot of the raw data; a large amount of data points from each dataset makes the plot almost unreadable. To better visualize the boxplots, the data were binned into 100 averaged bins (see Figure 14). The pore size area boxplots show how different the sample KGT2763 is from the other two AFIP6-MkII samples (Figure 14 (a)). It appears to be more similar to the L1P755 data with a broader range of data. KGT2763 and L1P755 both show outlier datapoints much higher than the rest of the data. KGT2763 exhibits FGP as high as ~9μm^2, while the highest value of L1P755 is ~5.75μm^2. 96A and 97A are significantly lower ranges, <2.5μm^2.

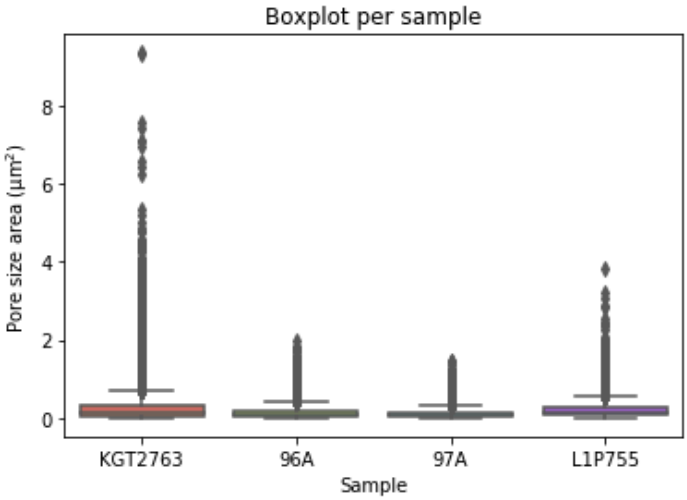

Figure 13. Boxplot of the raw pore size area data of each sample

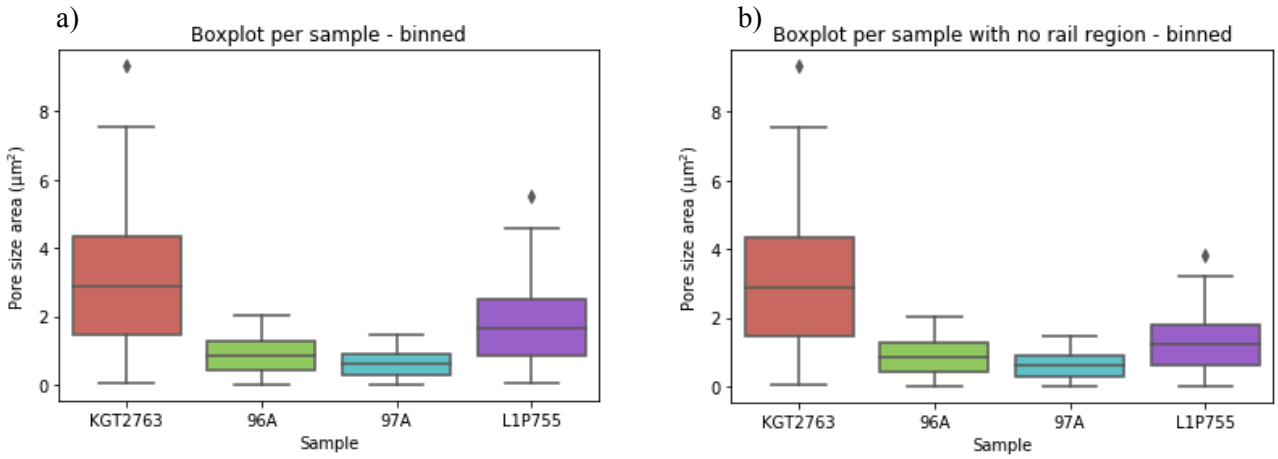

Figure 14. Boxplot of binned-average pore size area data of each sample

Table 7. Ranges of fission densities each sample is exposed to as referenced in the above boxplots

Sample	Minimum fission density ($x10^{21}$ f/cm^3)	Maximum fission density ($x10^{21}$ f/cm^3)	Maximum fission density – no rails ($x10^{21}$ f/cm^3)
KGT2763	3.89	4.50	4.25
96A	4.06	4.62	4.52
97A	3.74	4.05	NA
L1P755	4.45	6.23	5.37

As discussed previously, the rail regions restrict the pore size and morphology. Understanding the data without these locations is also important. However, the boxplot excluding these locations (Figure 14 (b)) still shows a large discrepancy between the KGT2763 sample and the others. Sample KGT2763 and 96A are not affected by the exclusion of the rail

regions noticeably. RERTR-12, L1P755, pore size area range decreases noticeably after the removal of the constrained, rail regions. The L1P755 range decreases when removing the rail regions. In these areas, the pore sizes are expected to be smaller because of the restricted growth. However, the pore size decreases when removing the rail regions. This indicates that the pore size area is larger in those locations, or there may be interconnected bubbles occurring in the rail regions of the RERTR-12 sample. Despite being constrained by the cladding rails, the fission density is the highest at these three locations out of all the data and could be overriding the constricted bubbles observed in the other rail regions.

5.2.2 Shape and normality of data

The distributions of pore size area at each fission density give a closer look into the behavior of the microstructure and FGP morphology. Frequency of small and large pores and viewing at what fission density these features appear is important for identifying when triggering mechanisms such as grain refinement and polygonization occur. To further understand the data collected via the automated pore size analysis, the normality of each dataset is investigated. As shown in the normalized relative frequency histograms presented in Figure 15 - Figure 18, the data is highly skewed to the right. It exhibits a bimodal distribution opposed to a standard bell curve. On the y-axis, the frequency is normalized to values of one. The limits of each plot are fixed to display the shape of the data more clearly. Smaller pores dominate the microstructure as indicated by the sharp peak on the far left. Samples KGT2763 and L1P755 have the most dramatic peaks (high kurtosis). 96A and 97A show a less dramatic peak, or a lower kurtosis, with a more widely distributed frequency spread of the data. For uniformity, each graph only shows pore size data up to 1.2μm^2 even though there are values higher than this area.

Based on the pore size areas range shown in the previous boxplots, there is a large spread in the size of pores. For example, on sample 95A at a fission density of $3.89 \times 10^{21} f/cm^3$, the largest observed pore is ~9μm^2. This is significantly higher than any of the other pore size maximums present at the other fission densities. The porosity of KGT2763 was the highest at 28% volume fraction, and in this sample, the porosity decreased with increasing fission density, as evidenced by Figure 11(b) above. A large portion of the pores at the lower fission densities extended to 3μm^2. Higher porosity values are associated with these areas with larger pores as well. However, none of the results achieve the 30% porosity value expected to predict the fully interconnected pores of metallic fuels [38]. Further analysis of these large pores will be done in future work to determine the amount of interconnection present in the samples with these larger pore sizes.

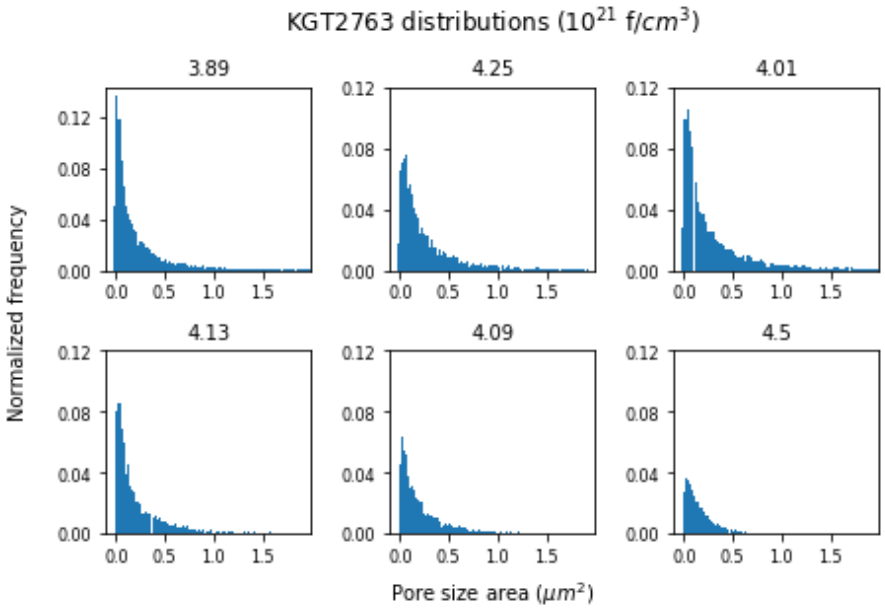

Figure 15. Normalized frequency (0-1) of AFIP-6MkII KGT2763

Distributions of 96A are different than those of KGT2763 (Figure 15) and shown in Figure 16. The 96A data appears to tail out to ≤ 0.7 μm^2 rather than the tailed region of KGT2763, which reaches past 1 μm^2 to 1.75 – 2.00 μm^2. The longer tail shows that KGT2763 had a higher count of larger pores than 96A. 97A and L1P755 showed the shorter tails similar to 96A.

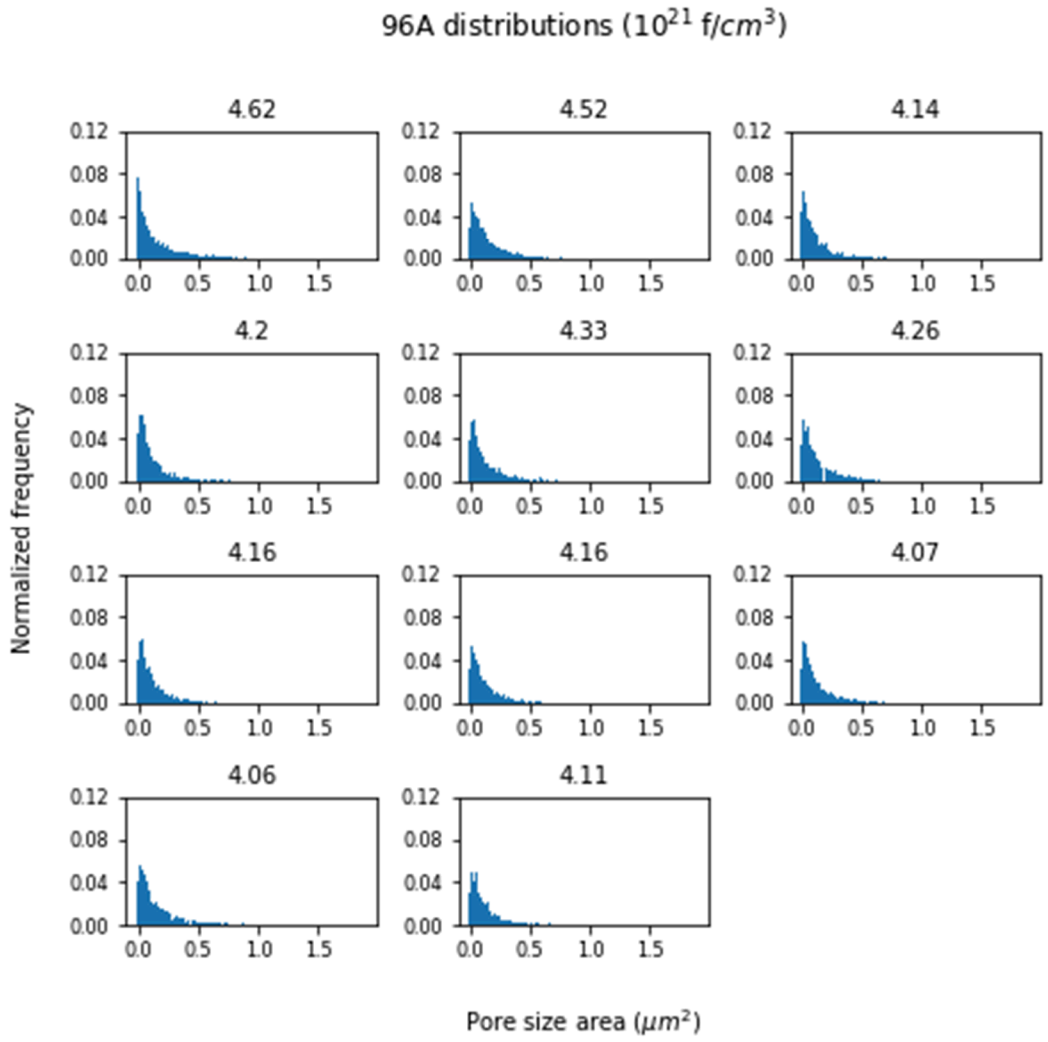

Figure 16. Normalized frequency (0-1) of AFIP-6MkII 96A

97A did not contain any rail regions, and therefore all the distributions presented in Figure 17 are representative of the behavior. Fission densities of 97A were lower than in the other three samples, and this corresponds to the slightly lower FGP size observed throughout 97A. However, 97A fission densities were all still above the estimated $3x10^{21}$f/cm^3 threshold for the onset of grain refinement.

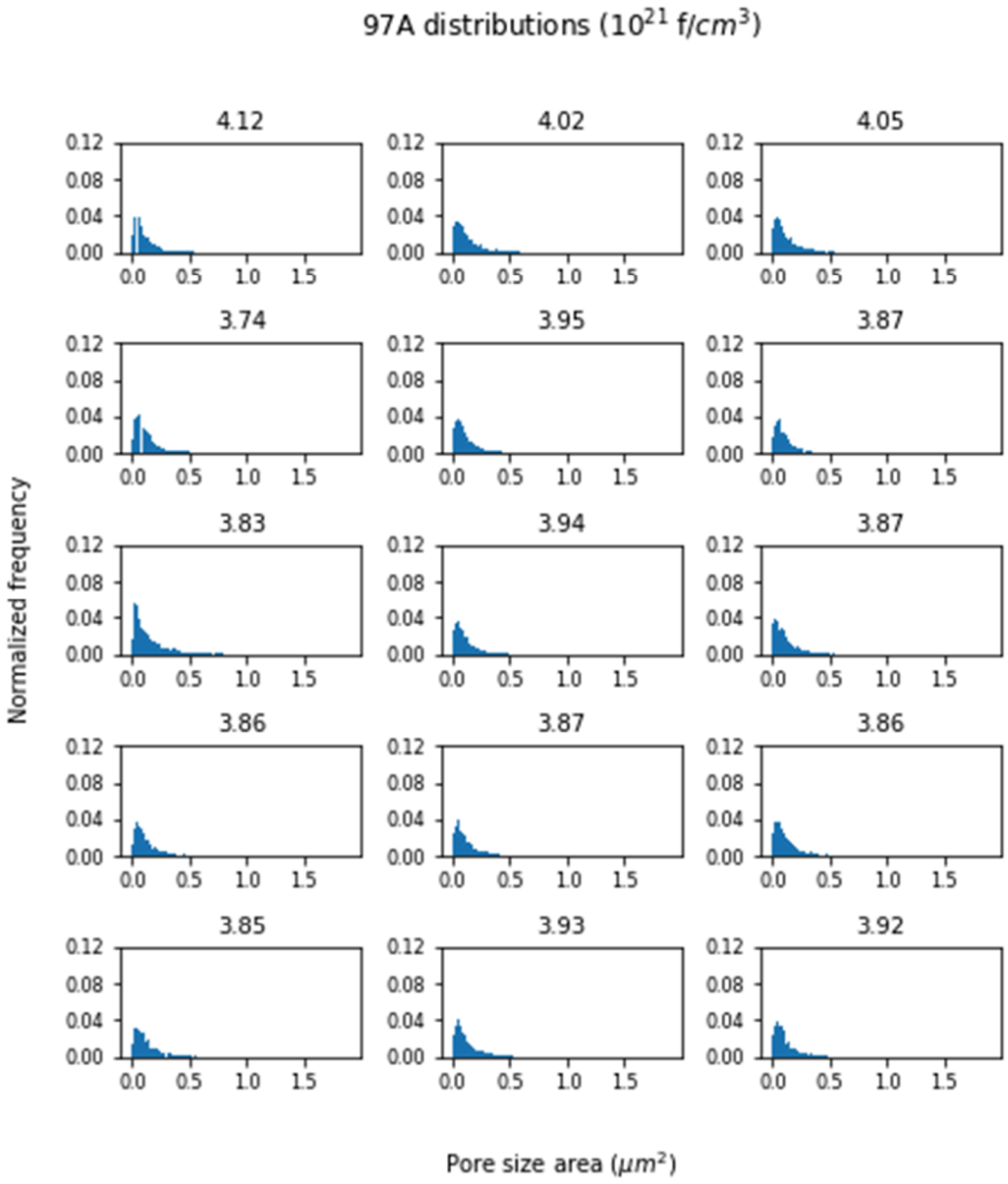

Figure 17. Normalized frequency (0-1) of AFIP-6MkII 97A

The normalized frequency of pore size area for the L1P755 sample is shown in Figure 15. The highest fission densities observed are in sample L1P755. Consequently, almost all the surface of this plate showed grain refinement. Tails of the histogram for the RERTR-12 data trail toward 1μm^2 and even past in some instances. KGT2763 appears to be the most similar AFIP6-MkII sample to L1P755 from this initial analysis. High peaks showing a large concentration of small pores are seen in the last three histograms of Figure 18. Data at these rail regions are smaller, as was predicted. However, this behavior at the rail regions was different from that seen in the KGT2763 rail regions.

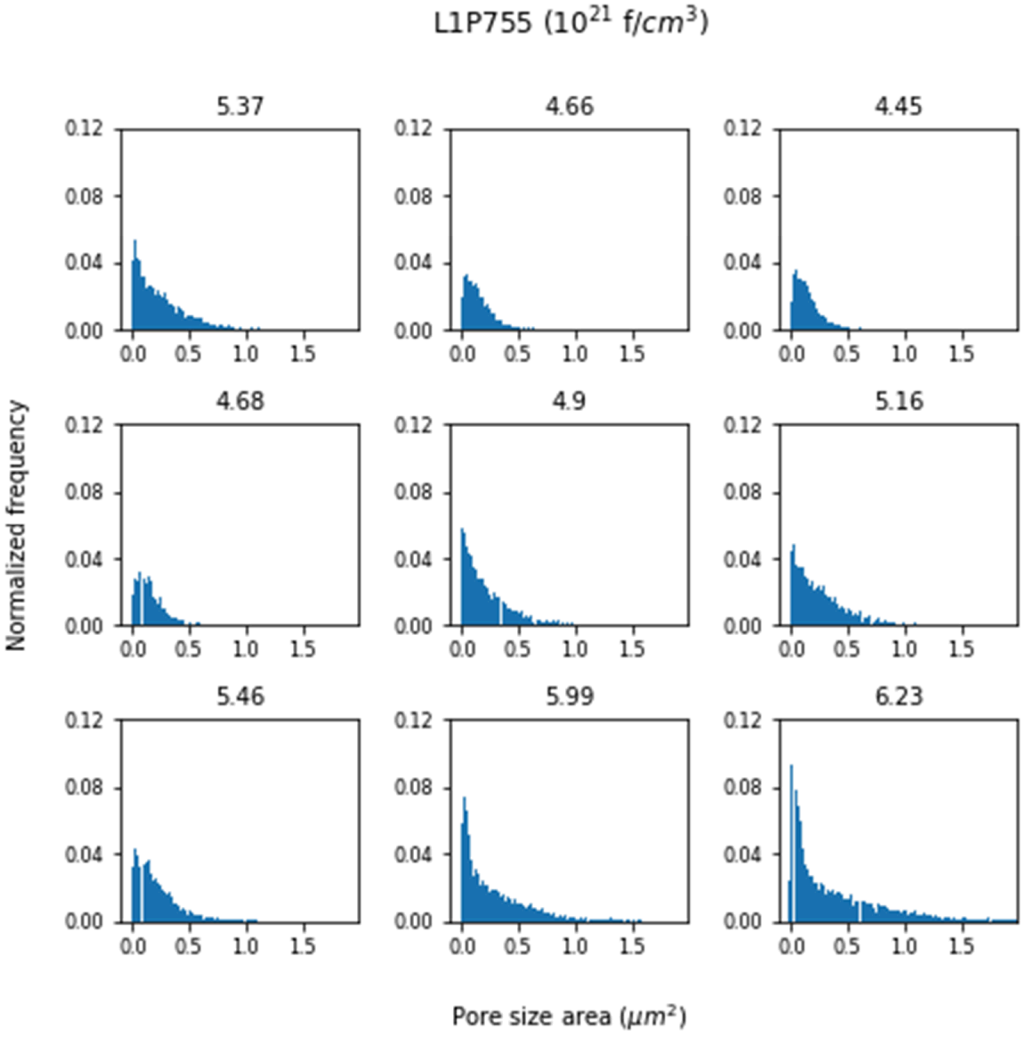

Figure 18. Normalized frequency (0-1) of RERTR-12 L1P755

SciPy, a Python statistics package, is used to perform the D'Agostino and Pearson's test for normality to verify the observations from the normalized frequency histograms are correct. Skew and kurtosis calculations create an omnibus test of normality. The output is in the format of s^2+k^2. S is the z-score from a skew test, and k is a z-score returned by a kurtosis test. The p-value, or the significance of the test results, is also calculated with a chi-squared probability test [36]. A significance level $\alpha = 0.05$ is applied. Therefore, if the p-value is less than α, the test rejects the null hypothesis that the data is normally distributed and determines the sample varies from a normal distribution. Results from the D'Agostino and Pearson's test confirms none of the datasets of pore size area have a normal shape. These two normality tests can be used on future data as well when the datasets do not visually show how non-normal the shape of the data is or is not. Visual inspection of data shape may be misleading at times and using a standard method to verify the results is important for a thorough analysis of the data. Understanding and confirming

the normality of the data sets will also indicate the need for further data transformation or what tests to use in future analysis.

5.2.3 Outliers and interconnected pores

Each micrograph has a different number of pores. Therefore, the datasets differ in length and contain outliers and errors. As shown in the histograms, data is not a normal distribution and follows a bimodal distribution in most cases. Outliers can cause the bimodal distribution. To explore the effects of these very high FGP values, outliers were removed, and the data summarized. Outliers were found using the method proposed in Chebyshev's inequality. This method calculates z-scores of each data point to determine how many standard deviations from the mean a point is. Chebyshev's inequality states that for a skewed probability distribution, only a fraction of the data is within a certain distance from the mean. At least $1/k^2$ of the distribution's values fall within 'k' standard deviations of the mean. For four standard deviations, 93.75% of the data is within that many standard deviations of the mean, i.e., 6.25% are outside that range (5 is 96%, and 3 is 88.9%). The data points outside of 93.75% of the distribution are considered outliers and are excluded in this analysis. To demonstrate the difference this makes, Table 8 compares the summary data analysis of the pore size area of point A (at $3.89x10^{21}$ f/cm^3) on KGT2763 before and after outlier removal. Without outliers, the number of actual data points for each sample decreases minimally, as does the mean. Most notably, the maximum value, skewness, and kurtosis decrease. A lower maximum value is evident since the largest values are treated as an outlying value. More importantly, the skewness and kurtosis values are much lower and closer to what is expected in a normal distribution. Ideally, the skew should be equal to 0, indicating the data distribution is equal below and above the mean. This sample had the most drastic change in average values for all the samples before and after removing the outliers. The mean is only different by ~13%. For this work, the outliers were determined not to be significant to the calculated mean and were left within the data. This was also true for the rail region areas. These constrained regions did not exhibit a noticeable change in mean pore size with the removal of outlying data points either.

Table 8. Comparison of raw data to 93.75% of data of KGT2763 FD $3.89x10^{21}$ f/cm^3

	Raw Data Summary	Outliers Removed
Number of data points (pore count)	7097	7011
Min	0.00074	0.00074
Max	9.34	2.17
Mean (μm^2)	0.277	0.241
Variance	0.231	0.103
Skewness	6.046	2.61
Kurtosis	66.0	8.04

Additionally, very large FGP need to be considered when using other analyses that require the data to be free of outliers and are evidence of pore interconnection. A concern with removing outliers is that pore size area values that are valid measurements are removed. The interconnection of bubbles will occur and create bubbles that are much larger than the smaller FGB created at the beginning of the microstructure evolution. It's estimated that pore

interconnection does not occur until porosity reaches 30%. The interconnection of pores indicates a release of fission gases [38]. Therefore, it's possible that the areas with the most outliers exhibited high amounts of pore interconnection, rather than errors in the image analysis. For this reason, for the non-normal distribution of each dataset, a method of data transformation was used.

5.2.4 Data transformation

Transforming the data into a normal distribution is a critical step in determining the best methods of analyzing and understanding the data further. It allows for the development of correlations and more detailed statistical tests. Many commonly used statistical methods require the data used have a normal distribution. By using non-normal datasets, the types of methods and tests are therefore limited. While there are many methods of transforming data, this study used the Box-Cox transformation developed in 1964 [39]. This method uses a value (λ) to transform a non-normally distributed dependent variable to create a normal distribution. Values of λ between -5 and 5 are tested in the equation below. The value of λ that estimates the closest to a normal distribution of y'(λ) is the transformation variable [39].

$$y'^{(\lambda)} = \begin{cases} \dfrac{y^{\lambda} - 1}{\lambda}, & if\ \lambda \neq 0; \\ log\, y, & if\ \lambda = 0 \end{cases}$$

Box-Cox transformations are calculated by many types of software that solve for the appropriate λ value. Python was used for these purposes. The normality of the pore size area from each dataset is shown below in a histogram and probability plot. Each is compared with the transformed data using the Box-Cox method. λ was estimated to be approximately 0.16. The change in the data after transformation is illustrated in a normalized frequency histogram. Figure 19 shows that the untransformed data shape is similar to the individual pore size area distributions presented previously. The data is right-skewed, with skewness values above 3. A distribution is highly skewed at values higher than one. After the Box-Cox transformation, the new shape of the data demonstrates a more normal shape in Figure 19. The skew of the data also decreases to approximately 0.005, indicating almost no skewness.

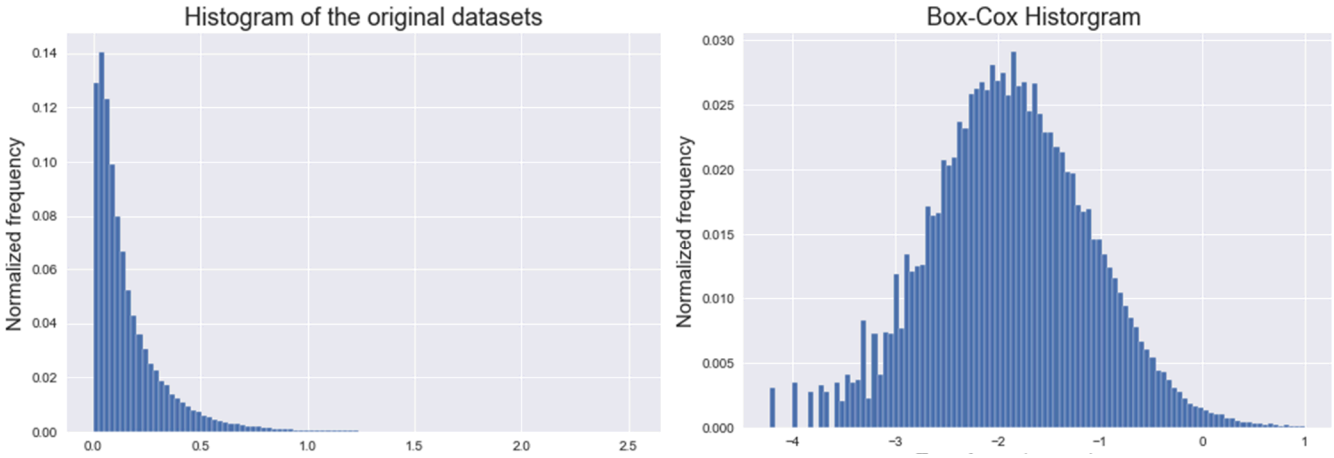

Figure 19. Normalized frequency of total combined datasets before and after Box-Cox transformation

Linear correlations were explored based on the average pore size area and the average transformed pore size area. However, there was little improvement in the R^2 value of each equation. A maximum R^2 of 0.73 was achieved using the transformed data. Table 9 shows the slope and y-intercept values of each case before and after the Box-Cox transformation.

Table 9. Slope and intercepts of pore size area dependent on fission density

Dataset	Slope (m)	y-intercept (b)	R^2	Skew
Raw data	8.38e-23	-0.193	0.702	3.26
Raw data without rails	8.34e-23	-0.189	0.522	3.45
Transformed data	2.89e-22	-3.12	0.729	0.0056
Transformed data w/o rails	3.44e-22	-3.34	0.627	0.0087

A linear relationship of the pore area is not the ideal method to use for finding a correlation to the fission density. However, as seen in Table 9 transforming the data with the Box-Cox transformation improves the skewness of the data (centers it towards the mean) and leads to a more reliable goodness-of-fit value (R^2).

Q-Q plots explore the normality of the data before and after transformation by plotting data points into their proper quantiles against a theoretical distribution [40]. In these plots, a straight line of the data points matching the red line indicates the dependent variable (pore size area) comes from a normally shaped distribution. Figure 20 supports this determination that the original data is not normally distributed. The curved, blue line is not close to the linear red line that would indicate the normality.

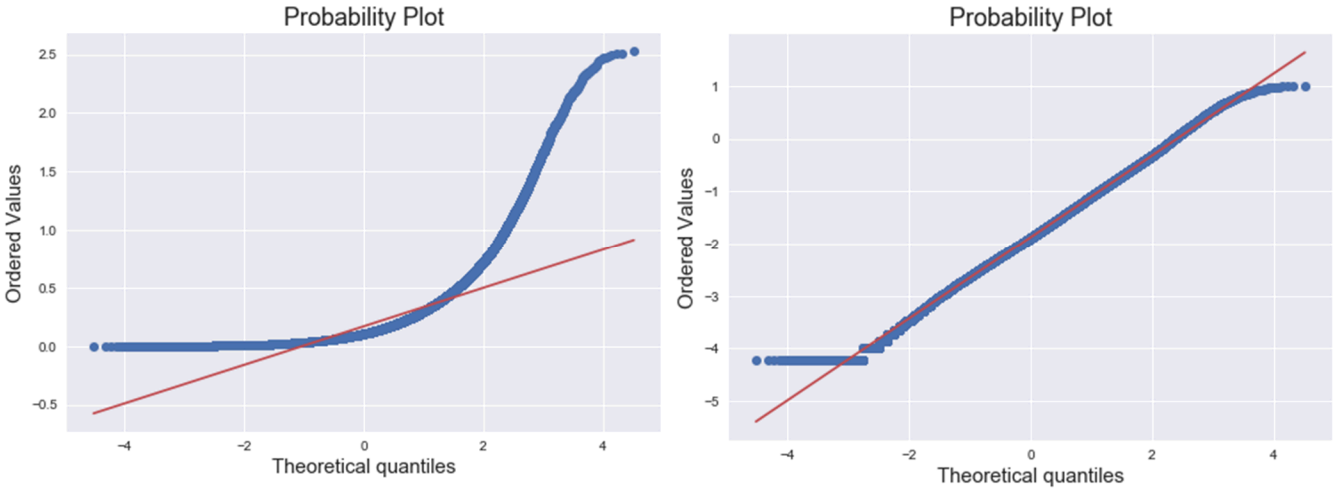

Figure 20. Q-Q plot of pore size area data before and after Box-Cox transformation

Figure 20 is the Q-Q plot of the transformed data. The tail ends deviating from the line indicate a distribution that has data points near the edges of the data, causing the distribution to be non-normal. The improvement of the normality from the transformation is better than the

untransformed data. Further types of transformation methods will be attempted to normalize the pore size area data better

5.2.5 Analysis of covariance

After transforming the data into a normal distribution, the ANOVA (analysis of variance) and ANCOVA (analysis of covariance) analyses are performed. ANCOVA measures if the behavior of the dependent variable is caused by more than one independent variable. Before completing the ANCOVA, the ANOVA for both independent variables (fission density and sample) is performed separately. The ANOVA will determine if each independent variable has a noticeable effect on the pore size area, assuming the two independent variables are not related. Another importance of testing the ANOVA of both independent factors is understanding what aspect of the fuel has the most impact on the pore size area. ANOVA is used as the starting point of investigating the fission density and a characteristic of the fuel microstructure in each sample are impactful on the pore size area, independently.

An ANOVA tests if an independent variable has a significant impact on the dependent variable [40]. The first ANOVA tested the transformed variables to see there was a significant difference between the pore size areas at the different fission densities. An F-value and a p-value are calculated in the ANOVA and will indicate if the sample means are equal and the significance of the result, respectively. The F-value is a ratio of the differences of the sample means and differences within the sample itself. An F-value value of one indicates the means are equal, but if the F-value is high, the differences seen between population means is not due to chance. Something is affecting the results and is causing the differences seen in the behavior. The ANOVA of the fission density and pore size area had a resulting F-value of 81.276 with a corresponding p-value less than 0.001. The values show the fission density does have a significant effect on the pore size area, as is expected. A second ANOVA tested if which sample the pore size data came from also affected the outcome. Results of 40.336 for the F-value and a p-value less than 0.001, confirm there is a characteristic of the sample area, also impacting the pore size area independent from the fission density. These results do show the effects of the fission density on the pore size area are more impactful than the sample areas.

An ANCOVA was used to explore the impacts of the covariate (fission density) and the categorical independent variable (sample) together. The previous ANOVA results looked at the impacts of the two variables on the pore size area separately. The ANCOVA looks to see if the variance of the fission density is controlled, and if the sample the data comes from still impact the pore size area [40]. In other words, it explores the impacts of both the fission density and the sample. Fission density is known to impact the pore size area already, and this method will look for the effects caused by a feature of the sample while still considering the fission density. The fission density and sample are assumed to be independent of one another, i.e., the independent variables are additive. Assumptions that the fission density and sample are independent were used to explore the possible effects of the sample itself and if there is a statistical basis in saying there is more to the pore development than just fission density. For example, if the pore effects are due to the beginning microstructure or a fabrication method, the fission density could be considered fully independent. However, if the two most impactful variables are fission density and grain refinement, they would not be considered independent. By completing future analysis

like this but selecting a particular sample characteristic (e.g. grain size or phase decomposition) the relationship can be better understood using this methodology.

The results of the ANCOVA are presented in Table 10. All of the results prove to be significant ($p<0.001$) if the fission density and sample are independent of each other. This is different from the ANOVA analysis in that the means are compared by separating them into the sample groups and comparing the fission densities with them. Previously, the means are either fully based on the fission density or to the sample, not both. Based on the F- and p-values, where the pore area is sampled from (F-value = 51.660, p = 3.99e-13) is more significant than the fission density (F-value = 15.186, p = 0.0004068). Fission density and effects from some characteristics unique to each sample would be independent of each other if the factor affecting pore size in each sample came from something like the starting microstructure or fabrication treatment. However, it's possible for a feature of the material also affected by the fission density, such as grain refinement, to impact the FPG growth as stated previously. Therefore, depending on the sample characteristics, the independent variables in the ANCOVA can be considered to have some interaction, both impacting the pore size.

Table 10. ANCOVA assuming no interaction between fission density and sample

Fission Density	Sum of squares	Degree of freedom	F-value	P-value	Significance level
Fission Density	0.16758	1	15.186	0.0004068	***
Sample	1.71023	3	51.660	3.998e-13	***
Residuals	0.39726	36			
Significance level codes: "***" ~ 0, "**" ~ 0.001, "*" ~ 0.05, "." ~ 0.1, blank is not significant					

Table 11 shows the results from the ANCOVA, assuming the interaction of the two independent variables (represented in the row "fission density & sample"). There is no impact of the fission density or the sample area on the pore size area according to this analysis. The F-values for the fission density and the sample were below one and the p-values were too high to be considered significant. Meaning, if the two variables are not independent from one another the fission density and the sample do not fully explain the differences seen in the sample. However, there appears to be a slightly significant (F-value = 3.2487, p-value= 0.0341) interaction between the two variables. In the "fission density" row the combination of the two variables' effects on the pore size area are more significant than either the fission density or sample alone.

Table 11. ANCOVA assuming interaction between fission density and sample

Fission Density	Sum of squares	Degree of freedom	F-value	P-value	Significance level
Fission Density	0.005731	1	0.6167	0.43790	
Sample	0.075002	3	2.6901	0.06221	.

Fission Density & Sample	0.090575	3	3.2487	0.03410	*
Residuals	0.306687	33			
Significance level codes: "***" ~ 0, "**" ~ 0.001, "*" ~ 0.05, "." ~ 0.1, blank is not significant					

To better understand effects of the samples, individual sample characteristics must be found and tested in the ANCOVA method used above. The first method that assumes independence of the covariate and the categorical independent variables can be used with the starting microstructure features. The second method assuming a connection between the two can be used with features dependent on the fission density. Other contributing factors like temperature and data are needed as well to better inform the future data analysis and to understand the fuel behavior based on changing conditions. To perform these other analyses with more precise sample characteristics and conditions more data of the microstructure pre- and post-irradiation is needed at the same locations the pore size area and porosity data are taken.

6. CONCLUSIONS

At times, a lack of available experimental and inconsistent types of microstructural data makes analysis and collection for microstructural models complicated. For example, in this work, the calculated fission densities used to analyze the materials did not overlap for several of the samples. This makes it difficult to understand the relationships between fission density and the pore features because the direct comparison of one sample to another is not ideal unless the same fission density was present. Having samples from various experiments with the same fission density would be ideal. Another difficulty in comparing the two experiments is possible error in the fission density calculations. The amount of error is unknown at this time and will be further elucidated in future studies. Despite the differences in the two experiments, whether it is from errors in fission density calculations or actual observable behavior, relationships or trends between the fission density and the microstructure can be explored. Finding existing correlations or relationships between each sample is a starting place for understanding the behavior better. That is why the ANOVA and ANCOVA tests were performed on the pore size area data. The stronger relationship is between the pore size area and the locations of the samples. Underlying mechanisms, therefore, are likely more influential to the microstructure behavior than the fission density. Future analysis is being performed to elucidate what those mechanisms may be. It could be related to almost anything in the material such as chemical composition, phase decomposition, or the starting microstructure [14].

Assuming the fabrication and compositions of all the AFIP6-MkII samples and RERTR-12 are reasonably similar, the behavior of the material should follow a similar pattern as the fission density increase. This was not the case for the samples investigated here. KGT2763 and L1P755 exhibited evidence of large interconnected pores while 96A and 97A did not show these large pore-like structures. More analysis must be done on these samples to understand if the structures are errors in the FGP-GUI analysis or interconnected pores. Of the samples in AFIP6-MkII, the highest values of porosity and pore size area are found in KGT2763. The FGP area of this sample is approximately 45 to 55% higher than the other two samples. 96A pores were about 18% higher than 97A.

Possible causes of data discrepancies:

- The heterogeneous material structure likely caused some of the discrepancies seen in the AFIP6-MkII samples.

- KGT2763 was a much smaller sample when compared to the other two AFIP6-MkII samples and was cut close to the constrained cladding, or rail regions. The smaller sample size could bias the results because the area available for micrographs was not as large.
- Data from rail regions also can affect the reliability of the results. The suppression of the FGB growth would decrease the porosity due to the constraining stresses applied to the fuel edges by the cladding. This behavior was not observed in 96A and RERTR-12, however. Rail regions here were measured to find the highest porosity and the highest fission density.
- In sample KGT2763, there appeared to be a high number of interconnected pores even though the porosity was not high enough for this to be occurring as expected. Interconnected pores, therefore, may be forming sooner than originally thought and affecting the results. The larger, possibly interconnected pores also could be due to the high temperatures experienced at the top of the AFIP6-MkII plate.

The overarching conclusion from the work presented is a need for more data on all the pore features and as-fabricated microstructure. To form more reliable correlations and data for modeling purposes, more data is needed before and after irradiation of material. With more data to work with, better predictions can be made as to how U-Mo alloy fuels behave under various conditions.

7. REFERENCES

[1] "Reduced Enrichment for Research and Test Reactors (RERTR) [Nonproliferation]." [Online]. Available: https://www.rertr.anl.gov/. [Accessed: 13-Apr-2020].

[2] J. Rest, Y. S. Kim, G. L. Holmes, M. K. Meyer, and S. L. Hayes, "U-Mo Fuels Handbook: Version 1.0," 2006.

[3] "U.S. HIGH PERFORMANCE RESEARCH REACTOR PRELIMINARY DESIGN MILESTONE FOR CONVERSION TO LOW ENRICHED URANIUM FUEL (Conference) | OSTI.GOV." [Online]. Available: https://www.osti.gov/biblio/1515073. [Accessed: 13-Apr-2020].

[4] M. L. Bleiberg, J. D. Eichenberg, R. H. Fillnow, and L. J. Jones L J Jones, "Development and Properties of Uranium-Base Alloys Corrosion Resistant in High Temperature Water," 1957.

[5] R. M. Willard and A. R. Schmitt, "Irradiation Swelling, Phase Reversion, and Intergranular Cracking of U-10wt% Mo Fuel Alloy," Canoga Park, CA, 1965.

[6] A. M. Casella, D. E. Burkes, P. J. MacFarlan, and E. C. Buck, "Characterization of fission gas bubbles in irradiated U-10Mo fuel," *Mater. Charact.*, vol. 131, pp. 459–471, Sep. 2017.

[7] C. A. Smith, D. D. Keiser, B. D. Miller, and A. Aitkaliyeva, "Comparison of manual and automated image analysis techniques for characterization of fission gas pores in irradiated U-Mo fuels," *Micron*, vol. 119, pp. 98–108, Apr. 2019.

[8] J.-F. Jue *et al.*, "RERTR-12 Characterization Summary Report," 2013.

[9] G. Moore and D. Fox, "RERTR-12 Fabrication Summary Report," Idaho Falls, Idaho, 2014.

[10] G. Moore, "AFIP-6MKII Fabrication Summary Report," Idaho Falls, Idaho, 2012.

[11] D. D. Keiser *et al.*, "Quantitative Image Analysis of AFIP6-MkII and RERTR-12 Fresh Fuel and Irradiated Fuel Fission Gas Bubble and Recrystallized Fraction," Idaho Falls, Idaho, 2018.

[12] F. Rice, W. Williams, A. Robinson, J. Harp, M. Meyer, and B. Rabin, "RERTR-12 Post-irradiation Examination Summary Report," 2015.

[13] W. Williams, F. Rice, A. Robinson, M. Meyer, and B. Rabin, "AFIP-6MKII Post-irradiation Examination Summary Report," 2015.

[14] A. Robinson, W. Williams, B. Rabin, J.-F. Jue, D. Keiser, and N. Lybeck, “Follow on Investigation of U-Mo Monolithic Fuel Swelling in the AFIP-6 MkII Experiment,” 2018.

[15] B. Ye, J. Rest, Y. Soo Kim, G. Hofman, and B. Dionne, “DART Analysis of Irradiation Behavior of U-Mo/Al Dispersion Fuels,” *Nucl. Technol.*, vol. 191, no. 1, pp. 27–40, 2015.

[16] S. Jana, N. Overman, T. Varga, C. Lavender, and V. V Joshi, “Phase transformation kinetics in rolled U-10 wt. % Mo foil: Effect of post-rolling heat treatment and prior γ-UMo grain size,” *J. Nucl. Mater.*, vol. 496, pp. 215–226, 2017.

[17] S. Hu, D. Burkes, C. A. Lavender, and V. Joshi, “Effect of grain morphology on gas bubble swelling in UMo fuels – A 3D microstructure dependent Booth model,” *J. Nucl. Mater.*, vol. 480, pp. 323–331, Aug. 2016.

[18] B. Beeler, Y. Zhang, and Y. Gao, “An atomistic study of grain boundaries and surfaces in γU-Mo,” *J. Nucl. Mater.*, vol. 507, pp. 248–257, 2018.

[19] M. K. Meyer *et al.*, “Irradiation Performance Of U-Mo Monolithic Fuel,” *Nucl. Eng. Technol.*, vol. 46, no. 2, pp. 169–182, Apr. 2014.

[20] Y. S. Kim, G. L. Hofman, and J. S. Cheon, “Recrystallization and fission-gas-bubble swelling of U-Mo fuel q,” *J. Nucl. Mater.*, vol. 436, pp. 14–22, 2013.

[21] B. Beeler, Y. Zhang, and Y. Gao, “An atomistic study of grain boundaries and surfaces in γU-Mo,” *J. Nucl. Mater.*, vol. 507, pp. 248–257, Aug. 2018.

[22] S. Neogy *et al.*, “Microstructural study of gamma phase stability in Uâ€“9wt.% Mo alloy,” *J. Nucl. Mater.*, vol. 422, pp. 77–85, 2012.

[23] J. Gan *et al.*, “TEM characterization of U-7Mo/Al-2Si dispersion fuel irradiated to intermediate and high fission densities,” *J. Nucl. Mater.*, vol. 424, no. 1–3, pp. 43–50, 2012.

[24] Y. S. Kim, G. L. Hofman, and J. S. Cheon, “Recrystallization and fission-gas-bubble swelling of U-Mo fuel,” *J. Nucl. Mater.*, 2013.

[25] J. Rest, “Evolution of fission-gas-bubble-size distribution in recrystallized U-10Mo nuclear fuel,” in *Journal of Nuclear Materials*, 2010, vol. 407, no. 1, pp. 55–58.

[26] J. Gan, D. D. Keiser, B. D. Miller, J. F. Jue, A. B. Robinson, and J. Madden, “TEM characterization of irradiated U-7Mo/Mg dispersion fuel,” *J. Nucl. Mater.*, vol. 494, pp. 380–397, 2017.

[27] J. Gan *et al.*, “Irradiated microstructure of U-10Mo monolithic fuel plate at very high fission density,” *J. Nucl. Mater.*, vol. 492, pp. 195–203, Aug. 2017.

[28] S. Neogy *et al.*, “Microstructural study of gamma phase stability in U–9 wt.% Mo alloy,” *J. Nucl. Mater.*, vol. 422, no. 1–3, pp. 77–85, Mar. 2012.

[29] “ASTM E562-11 - Standard Test Method for Determining Volume Fraction by Systematic Manual Point Count.” [Online]. Available: https://webstore.ansi.org/standards/astm/astme56211. [Accessed: 07-Jul-2020].

[30] Y. Soo Kim, G. L. Hofman, J. S. Cheon, A. B. Robinson, and D. M. Wachs, “Fission induced swelling and creep of U-Mo alloy fuel,” *Journal of Nuclear Materials*, 2013. [Online]. Available: https://reader.elsevier.com/reader/sd/pii/S0022311513003899?token=302EACACDA82655E006ABF8820617B7624F5E119403A3EBF2380C5F50402F593E16D2BCE55289FFAF125EDFE41788F1F. [Accessed: 07-Jul-2020].

[31] X. Jian, F. Yan, X. Kong, and S. Ding, “Effects of U-Mo irradiation creep coefficient on the mesoscale mechanical behavior in U-Mo/Al monolithic fuel plates,” *Nucl. Mater. Energy*, vol. 21,

Dec. 2019.

[32] D. M. Perez, J. W. Nielsen, G. S. Chang, D. M. Wachs, and N. E. Woolstenhulme, “AFIP-6 Mark II Irradiation Summary Report,” no. September 2012.

[33] Astm, “Standard Test Method for Determining Volume Fraction by Systematic Manual Point Count,” *Practice*, no. C, pp. 1–7, 2011.

[34] R. Collette, “Fission Gas Pore Analysis GUI User ’ s Manual,” 2015.

[35] “R: The R Project for Statistical Computing.” [Online]. Available: https://www.r-project.org/. [Accessed: 21-Apr-2020].

[36] “Statistical functions (scipy.stats) — SciPy v1.4.1 Reference Guide.” [Online]. Available: https://docs.scipy.org/doc/scipy/reference/stats.html. [Accessed: 21-Apr-2020].

[37] T. Sweijen, S. M. Hassanizadeh, H. Aslannejad, and S. Leszczynski, “The effect of particle shape on porosity of swelling granular materials: Discrete element method and the multi-sphere approximation,” *Powder Technol.*, vol. 360, pp. 1295–1304, Jan. 2020.

[38] W. J. Carmack *et al.*, “Metallic fuels for advanced reactors,” *J. Nucl. Mater.*, vol. 392, pp. 139–150.

[39] G. E. P. Box and ; D R Cox, “An Analysis of Transformations,” 1964.

[40] R. M. Heiberger and B. Holland, “Springer Texts in Statistics Statistical Analysis and Data Display An Intermediate Course with Examples in R Second Edition.”

Appendix A Summarized pore size area

FD	count	mean	std	min	25%	50%	75%	max
3.89	7097	0.27690101	0.48021712	0.00073842	0.04504372	0.12257798	0.31309074	9.3439863
4.25	3719	0.30745975	0.40361226	0.00073842	0.07458058	0.16614485	0.37511815	4.78718691
4.01	6039	0.35974873	0.54475604	0.00147684	0.07088847	0.16762169	0.41831581	7.54371456
4.13	5612	0.26797584	0.36005069	0.00147684	0.05759688	0.13956167	0.3426276	4.3345345
4.09	5562	0.23552979	0.25513908	0.00073842	0.05907372	0.14546905	0.31752127	1.87263705
4.5	7200	0.16969727	0.15346777	0.00147684	0.0583353	0.12183956	0.23703332	1.39487831
4.62	5210	0.16789353	0.19866551	0.00073842	0.03027528	0.09451796	0.23241818	1.34761933
4.52	4290	0.15342352	0.17283035	0.00073842	0.03987476	0.09525638	0.20601961	1.97823133
4.14	4293	0.13303508	0.16484922	0.00073842	0.03175213	0.07679584	0.16614485	1.73159854
4.20	4701	0.14421007	0.18277134	0.00073842	0.03322897	0.08048795	0.18017486	1.8364544
4.33	4270	0.14819982	0.17265146	0.00073842	0.03470581	0.08787216	0.19789698	1.47167415
4.26	4795	0.15488819	0.17732571	0.00073842	0.03913634	0.09304112	0.20786567	1.50933365
4.16	4660	0.14727564	0.17305762	0.00073842	0.0376595	0.08934901	0.1882975	1.73676749
4.16	3632	0.13809642	0.15468047	0.00073842	0.03692108	0.08787216	0.18478999	2.03582821
4.07	4918	0.14620056	0.16713089	0.00073842	0.0376595	0.09008743	0.1919896	1.5041647
4.06	2381	0.16791228	0.18663899	0.00073842	0.03987476	0.10190217	0.22595699	1.5418242
4.11	5129	0.13019629	0.14079102	0.00073842	0.03544423	0.08344164	0.17574433	1.80174858
4.12	5871	0.11131148	0.10725627	0.00073842	0.03839792	0.07827268	0.14768431	1.22282609
4.02	5579	0.12614223	0.11778567	0.00073842	0.04652056	0.09304112	0.16688327	1.08991021
4.05	4905	0.12277685	0.11466867	0.00073842	0.04504372	0.08713374	0.16171432	1.03083648
3.74	5909	0.13135294	0.126138	0.00073842	0.0479974	0.09304112	0.1713138	1.45321361
3.95	6100	0.12282141	0.11710372	0.00073842	0.04430529	0.08713374	0.16023748	1.19550449
3.87	4620	0.10590579	0.09116129	0.00073842	0.04356687	0.07901111	0.14103852	0.66900992
3.83	4963	0.15134562	0.16435528	0.00073842	0.04135161	0.09304112	0.20085066	1.45099835
3.94	6429	0.10961925	0.09972006	0.00073842	0.04282845	0.08122637	0.1439922	1.03895912

3.87	5673	0.1157864	0.11152753	0.00073842	0.03987476	0.08122637	0.15359168	0.99982278
3.86	4881	0.12139402	0.11214781	0.00073842	0.04504372	0.08787216	0.15802221	0.87502954
3.87	4459	0.11659029	0.10565303	0.00073842	0.04652056	0.08418006	0.15285326	0.89570534
3.86	5978	0.12163364	0.11473643	0.00073842	0.04356687	0.08639532	0.1609759	1.14012287
3.85	7562	0.11884339	0.11219798	0.00073842	0.04282845	0.0856569	0.15728379	1.03009806
3.93	6109	0.11905256	0.10801908	0.00073842	0.04504372	0.08713374	0.15876063	1.01532963
3.92	5945	0.11221871	0.1043185	0.00073842	0.04209003	0.08048795	0.14768431	1.02566753
5.37	5694	0.27335444	0.26355276	0.00073443	0.07931787	0.20013073	0.38924509	3.08164599
4.66	7357	0.16552846	0.14553055	0.00073443	0.06462937	0.12852432	0.22253068	1.98000896
4.45	7757	0.16230539	0.13996026	0.00073443	0.0653638	0.1277899	0.21518643	1.6539244
4.68	5849	0.17068211	0.14498529	0.00073443	0.0712392	0.13586857	0.22767165	1.71488165
4.90	5403	0.25959718	0.27343457	0.00146885	0.07197362	0.1784652	0.35546155	3.80431989
5.16	4148	0.28276926	0.26397725	0.00146885	0.08813096	0.21298316	0.39603851	2.55139137
5.46	5213	0.23361693	0.22985088	0.00073443	0.08445884	0.17479308	0.30478625	2.32812626
5.99	5025	0.30542567	0.31783487	0.00146885	0.06683265	0.20196679	0.43992039	2.40744413
6.23	4453	0.4014458	0.46402462	0.00073443	0.07417689	0.23354705	0.58533648	5.53168675

Appendix B Summarized pore diameter, porosity, and eccentricity

FD	Porosity (%)	Porosity S.D.	Diameter (μm)	Diameter S.D.	Eccentricity	Eccentricity S.D.
KGT2763						
3.89	28.907	0.374	0.34	0.003	0.672	0.004
4.25	24.613	0.518	0.538	0.003	0.651	0.005
4.01	26.722	2.627	0.566	0.043	0.646	0.007
4.13	21.581	0.768	0.499	0.02	0.647	0.006
4.09	22.559	0.622	0.481	0.013	0.608	0.007
4.5	21.04	0.54	0.422	0.012	0.578	0.003
96A						
4.62	18.792	0.639	0.391	0.009	0.698	0.009
4.52	14.14	2.055	0.385	0.017	0.68	0.023
4.14	12.269	2.504	0.352	0.03	0.7	0.01
4.2	14.564	0.873	0.366	0.013	0.703	0.003
4.33	13.595	0.606	0.375	0.01	0.707	0.01
4.26	15.955	2.018	0.387	0.036	0.689	0.014
4.16	14.744	2.467	0.376	0.034	0.687	0.004
4.16	14.367	0.814	0.367	0.016	0.695	0.007
4.07	15.447	0.763	0.376	0.006	0.679	0.007
4.06	17.178	0.447	0.402	0.011	0.673	0.001
4.11	14.346	0.82	0.358	0.011	0.679	0.008
97A						
4.12	13.161	1.465	0.333	0.012	0.655	0.004
4.02	15.529	3.37	0.359	0.017	0.662	0.015
4.05	17.323	1.122	0.358	0.011	0.651	0.006
3.74	16.745	3.387	0.368	0.028	0.65	0.007
3.95	16.164	2.407	0.357	0.023	0.65	0.006
3.87	14.075	2.516	0.337	0.006	0.607	0.009
3.83	16.205	1.164	0.386	0.142	0.651	0.006
3.94	15.204	1.306	0.34	0.007	0.642	0.01
3.87	14.171	1.785	0.345	0.006	0.65	0.004
3.86	17.044	1.027	0.356	0.009	0.636	0.011
3.87	14.955	0.869	0.351	0.01	0.615	0.004
3.86	15.687	1.648	0.357	0.019	0.619	0.014
3.85	15.511	2.446	0.351	0.009	0.648	0.005

3.93	16.148	1.263	0.357	0.007	0.645	0.007
3.92	14.393	1.653	0.343	0.013	0.643	0.012
L1P755						
5.37	26.99	1.07	0.528	0.015	0.652	0.014
4.66	21.12	0.55	0.422	0.019	0.6	0.008
4.45	21.83	0.9	0.42	0.026	0.602	0.005
4.68	21.64	0.22	0.43	0.009	0.603	0.008
4.9	23.76	1.25	0.503	0.024	0.63	0.003
5.16	25.65	0.61	0.54	0.011	0.648	0.02
5.46	26.4	1.21	0.5	0.048	0.651	0.01
5.99	26.62	1.47	0.547	0.021	0.62	0.012
6.23	31	0.9	0.613	0.015	0.608	0.006